

# Topological Semimetals from first-principles

Heng Gao,<sup>1</sup> Jörn W. F. Venderbos,<sup>2,3</sup> Youngkuk Kim,<sup>4</sup> and Andrew M. Rappe<sup>2</sup>

<sup>1</sup>International Centre for Quantum and Molecular Structures, Department of Physics, Shanghai University, 99 Shangda Road, Shanghai 200444, China

<sup>2</sup>Department of Chemistry, University of Pennsylvania, Philadelphia, Pennsylvania 19104-6323, USA

<sup>3</sup>Department of Physics and Astronomy, University of Pennsylvania, Philadelphia, Pennsylvania 19104-6396, USA

<sup>4</sup>Department of Physics, Sungkyunkwan University, Suwon 440-746, Korea

Xxxx. Xxx. Xxx. Xxx. YYYY. AA:1-29

This article's doi:  
10.1146/((please add article doi))

Copyright © YYYY by Annual Reviews.  
All rights reserved

## Keywords

Topological semimetals, Dirac and Weyl fermions, multifold band crossings, nodal line semimetals, first-principles calculations, materials prediction

## Abstract

We review recent theoretical progress in the understanding and prediction of novel topological semimetals. Topological semimetals define a class of gapless electronic phases exhibiting topologically stable crossings of energy bands. Different types of topological semimetals can be distinguished based on the degeneracy of the band crossings, their codimension (*e.g.* point or line nodes), as well as the crystal space group symmetries on which the protection of stable band crossings relies. The dispersion near the band crossing is a further discriminating characteristic. These properties give rise to a wide range of distinct semimetal phases such as Dirac or Weyl semimetals, point or line node semimetals, and type-I or type-II semimetals. In this review we give a general description of various families of topological semimetals with an emphasis on proposed material realizations from first-principles calculations. The conceptual framework for studying topological gapless electronic phases is reviewed, with a particular focus on the symmetry requirements of energy band crossings, and the relation between the different families of topological semimetals is elucidated. In addition to the paradigmatic Dirac and Weyl semimetals, we pay particular attention to more recent examples of topological semimetals, which include nodal line semimetals, multifold fermion semimetals, triple-point semimetals. Less emphasis is placed on their surface state properties, responses to external probes, and recent experimental developments.

## 1. INTRODUCTION

The discovery of topological insulators (TIs) firmly established the notion of topology as a means to sharply distinguish electronic phases and classify quantum states of matter (1, 2). Classification schemes based on the topology of the ground state wave function—initially applied to electronic phases with an energy gap—have since been extended to gapless systems (3). This has led to the identification of a new and special class of metals: the topological semimetals (TSMs). TSMs are characterized by a topologically stable Fermi surface originating from a crossing of energy bands. Band crossings of this kind can be associated with a topological number, which may depend on the symmetries responsible for enforcing or protecting the band crossing degeneracy.

Different types of TSMs can be distinguished based on key attributes of the band crossing, such as its degeneracy, the codimension (*i.e.* whether the band degeneracy occurs at a point or on a line), and the dispersion in the vicinity of the crossing. Another possible distinction can be made based on the origin of the crossing, that is to say, whether it is symmetry-enforced or arises as a result of a band inversion. These attributes, in combination with their topological characteristics, have led to the identification of a growing number of different TSM families, which include Dirac and Weyl semimetals (4, 5, 6, 7), nodal line semimetals (8, 9, 10), type-I and type-II semimetals (11), multifold fermion semimetals (12, 13), and “triple-point” semimetals (14, 15, 16, 17), among others.

Topological semimetals can host a variety of different low-energy excitations, which not only offer promising potential for future applications but also offer a new platform for the fundamental study of novel quasiparticles beyond the standard paradigm of known particles in high-energy physics (13). Due to the nontrivial topology of the bulk and surface electronic states, topological semimetals are expected to exhibit intriguing quantum transport properties, such as unusual magnetoresistance and the chiral anomaly (18, 19, 20, 21, 22), which have attracted broad attention from both theoretical and experimental communities. Furthermore, topological semimetals are of interest due to their potential future application in chemical catalysis (23, 24), quantum computation (25), and spintronics (26).

In this review we present an overview of the recent progress—mainly from the theoretical frontier—in understanding and predicting novel types of TSMs, with an emphasis on first-principles electronic structure calculations. In the past few years, this field has witnessed a rapid development, ranging from the advancement of conceptual ideas to specific predictions of new materials. First-principles calculations have played an important role in this development by providing guidance and support in the search for new topological materials in general and TSMs in particular. A further aim of this review is to convey the central pillars on which the theory of topological semimetallic phases rests, paying particular attention to the connections and relationships that exist between different families of TSMs. A particularly useful theme which makes these connections transparent is the notion of symmetry. The symmetry properties of solid state materials are determined by their crystal and compositional structure and in turn determine the degeneracies and crossings of energy bands. Symmetry therefore naturally relates structural and electronic characteristics. As a result, the symmetries of the crystal lattice, *i.e.* the symmetries of the space group in combination with time-reversal ( $\mathcal{T}$ ) symmetry, are of fundamental importance for TSMs and provide an important underpinning for the theory of TSMs.

Over the past decade, the symmetry analysis of electronic energy bands has been supplemented with an equally powerful and consequential concept: band topology. Electronic phases can be sharply distinguished based on the topological properties of the ground state wavefunction, or, more precisely, the topology of the mapping from the Brillouin zone to the space of wave functions. In particular, insofar as TSMs are concerned, band crossings can typically be associated with a formal topological index, which is sensitive to the symmetries of the system, and this index gives rise to the notion of topological stability.

The implications of symmetry and topology are exemplified by two canonical examples of TSMs: the Weyl and Dirac semimetal. Even without any symmetry, a degeneracy of two energy bands may generically be expected to occur (*i.e.*, without fine-tuning) at a point in the three-dimensional Brillouin zone (27). The dispersion away from the touching point is generically linear and this defines a Weyl point or Weyl node, which, as discussed in more detail in Section 3, is characterized by a topological invariant called the Chern number (6). The Chern number protects the Weyl point in the sense that the degeneracy cannot be removed unless two Weyl points with opposite Chern number are brought to coincidence at the same momentum, by tuning Hamiltonian parameters or breaking translation symmetry, allowing them to hybridize. When  $\mathcal{T}$  symmetry and inversion ( $\mathcal{P}$ ) symmetry are present all energy bands are twofold degenerate and Weyl point degeneracies must come in pairs of opposite Chern number at the same momentum. Without further (crystalline) symmetries, however, the Weyl points are still allowed to hybridize, leading to an avoided crossing. To protect a fourfold-degenerate merger of two Weyl points, and thereby stabilize a Dirac semimetal phase, additional symmetries must present, such as rotation symmetry or nonsymmorphic space group symmetries. The stability of a rotation-symmetry protected Dirac point can be formally expressed in terms of a topological number built from energy band rotation eigenvalues (28).

These considerations serve to illustrate the significance of both symmetry and topology for TSMs. In general, the quantized topological numbers associated with the stability of TSMs depend on the type of band crossing and symmetry class. In many cases the topological properties of TSMs can be diagnosed by calculating momentum space Berry phases and Wilson loops (29), which have become standard tools of topological band theory. In other cases a formal topological number can be defined in terms of energy band symmetry quantum numbers. Many of these tools have been implemented in *ab initio* band structure calculations (30, 31, 32). Density functional theory (DFT) within the single particle approximation provides a good description of weakly correlated electronic systems and has proven to be instrumental in finding material realizations of TSMs. Recent illustrative examples include the Weyl semimetal TaAs (7, 33), the “triple-point” semimetals MoP (34) and WC (35), and the Dirac nodal line semimetal ZrSiS (36). The implementation of computational schemes to calculate topological quantities such as Berry phases has been particularly important for predicting TSMs, as they can be used to detect band crossings at generic non-high-symmetry momenta.

We begin by reviewing the basic aspects of Dirac and Weyl semimetals in the next two sections. We then turn to a discussion of nodal line semimetals, after which we proceed to a survey of a number of more recently introduced families of TSMs. In the final section, before a summary and outlook, we consider some recent developments in the systematic search for new topological materials, in particular novel TSMs. In an appendix we include a table collecting candidate materials which have been proposed; some but not all are discussed in the text.

Before we proceed, we feel compelled to point out the limitations inherent in reviewing a branch of condensed matter materials science as vast and diverse as TSMs. Our review covers a number of the recent developments but not all. In addition, the perspective and emphasis we choose is far from the only possible perspective one may adopt. In this regard, we note that a number of excellent longer and shorter reviews already exist in the general area of gapless topological materials (37, 38, 39, 40, 41, 42, 26, 30, 43, 44, 45, 3, 31, 46, 47, 48, 49, 32).

## 2. DIRAC SEMIMETALS

The Dirac Hamiltonian plays a central role in the theory of topological materials. Its significance follows from the fact that in the presence of  $\mathcal{T}$  and  $\mathcal{P}$  symmetry a three-dimensional Dirac fermion appears at the topological phase boundary between a normal insulator and a topological insula-

tor (50). To illustrate this in more detail, consider the Dirac Hamiltonian in three dimensions given by

$$H(\mathbf{k}) = \begin{pmatrix} m & v\mathbf{k} \cdot \boldsymbol{\sigma} \\ v\mathbf{k} \cdot \boldsymbol{\sigma} & -m \end{pmatrix} = v\mathbf{k} \cdot \boldsymbol{\sigma}\tau_x + m\tau_z, \quad (1)$$

where  $\mathbf{k} = (k_x, k_y, k_z)$  is momentum,  $v$  is a velocity (in condensed matter referred to as the Fermi velocity  $v_F$ ), and  $m$  is a mass;  $\boldsymbol{\sigma} = (\sigma_x, \sigma_y, \sigma_z)$  and  $\boldsymbol{\tau} = (\tau_x, \tau_y, \tau_z)$  are the two sets of Pauli matrices, which can be viewed as spin and orbital degrees of freedom, respectively. The mass parameter  $m$  controls the topological transition: when  $m$  is tuned such that it changes sign, the topology of the ground state changes. A sign change of  $m$  in Eq. (1) corresponds to a band inversion at a  $\mathcal{T}$ -invariant momentum and thus describes the transition between a normal insulator and a topological insulator. At the critical point of the transition, defined by  $m = 0$ , the spectrum of (1) is gapless at  $\mathbf{k} = 0$ , giving rise to a fourfold-degenerate point node with linear dispersion. As a result, at the critical point the low-energy electronic excitations are governed by a massless Dirac equation.

This is reminiscent of the low-energy electronic structure of graphene, which is described by a Dirac equation in two dimensions (51). The experimental realization of graphene (52) and the observation of the remarkable properties of Dirac electrons (51) have made it a paradigmatic example of condensed matter realizations of Dirac physics, and have inspired the attempt to generalize the realization of low-energy Dirac fermions to three dimensions. The critical point of a topological transition provides one possible realization, however, as is clear from Eq. (1), this requires a fine-tuning of Hamiltonian parameters to achieve a bulk gap closure. One possible yet experimentally challenging route is to tune the chemical compositions in materials such as  $\text{Bi}_{2-x}\text{In}_x\text{Se}_3$ ,  $\text{Pb}_{1-x}\text{Sn}_x\text{Se}$ ,  $\text{Pb}_{1-x}\text{Sn}_x\text{Te}$ ,  $\text{Bi}_{1-x}\text{Sb}_x$ , and  $\text{Hg}_{1-x}\text{Cd}_x\text{Se}$ , for which the critical point corresponds to specific values of  $x$ . First-principles calculations have predicted that this type of Dirac semimetal should occur in the materials  $\text{ZrTe}_5$  (53) and  $\text{SrSn}_2\text{As}_2$  (54), but its experimental verification has proven difficult (55, 56, 57, 58) as a result of sensitivity to factors such as temperature, pressure, and composition homogeneity.

The intrinsic instability of the Dirac point at the topological phase boundary has led to the search for a novel type of Dirac point stabilized by crystalline symmetries. Semimetallic phases hosting stable Dirac points define true Dirac semimetals. To date, two mechanisms have been identified for the realization of stable Dirac points, giving rise to two types of Dirac semimetals. The first kind, referred to as nonsymmorphic Dirac semimetals, relies on the nonsymmorphic nature of the crystal space group, enforcing the occurrence of Dirac points at high-symmetry points of the Brillouin zone boundary (4). The second kind, referred to as topological Dirac semimetals, relies on a band inversion in the presence of an  $n$ -fold rotational symmetry axis for  $n = 3, 4$ , and  $6$ , where the Dirac points appear in pairs off a high-symmetry momentum (5).

The Dirac semimetals in three dimensions have strong spin-orbit coupling and, importantly, the Dirac points are stable in the presence of spin-orbit coupling. This should be contrasted with the case of graphene, which strictly speaking is a (topological) insulator when spin-orbit coupling is accounted for (59, 60). In the remainder of this section, we discuss the three-dimensional Dirac semimetals in detail.

## 2.1. Symmetry-enforced and band inversion induced Dirac semimetals

The symmetry-enforced *nonsymmorphic* Dirac semimetal was first proposed by Young *et al.* (4), who examined the conditions under which the symmetries of the crystal space group mandate fourfold degeneracies with linear dispersion. It was found that such fourfold degeneracies, which are associated with four-dimensional irreducible (co)representations of the little group, can only occur in the case of nonsymmorphic space groups, and must be located at high-symmetry momenta

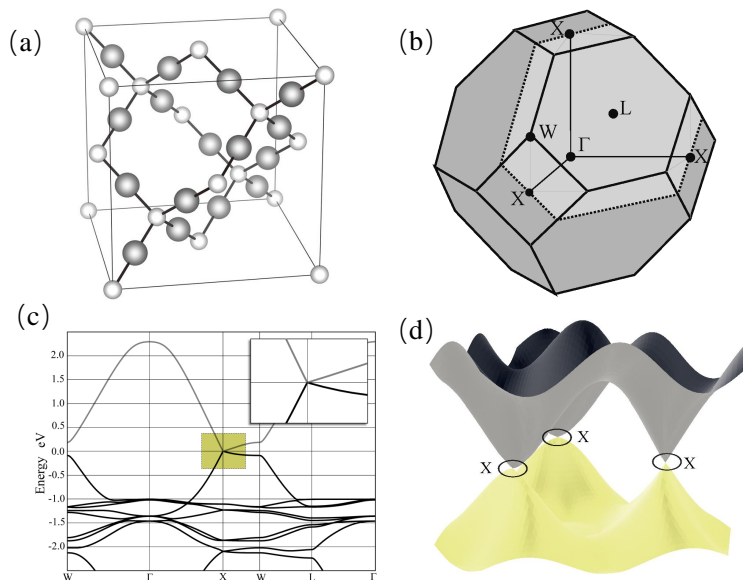


**Figure 1**

**Symmetry-enforced Dirac semimetal.** A nonsymmorphic symmetry-enforced Dirac semimetal phase was theoretically proposed to exist in  $\beta$ -cristobalite  $\text{BiO}_2$ , of which the  $\text{SiO}_2$ -type crystal structure is shown in (a). Here, bismuth atoms (light gray) are arranged on a diamond lattice, with oxygen atoms (dark gray) sitting midway between pairs of bismuth. Panel (b) shows the Brillouin zone of the FCC lattice; the plane highlighted in gray joins the three symmetry related X points. Other high-symmetry points are also indicated. The band structure of  $\text{BiO}_2$  in the  $\beta$ -cristobalite structure is shown in (c) and (d) shows the conduction and valence bands of  $\beta$ -cristobalite  $\text{BiO}_2$  plotted as functions of momentum in the plane, which touch at the Dirac points. Adapted from Ref. (4)

on the Brillouin zone boundary. Based on this general analysis a full list of space groups which admit such four-dimensional irreducible representations at high-symmetry points was obtained (61), revealing that 69 nonsymmorphic space groups can host symmetry-enforced Dirac points at a zone corner.

To realize the nonsymmorphic Dirac semimetals in real materials, it is desirable that the fourfold-degenerate Dirac point is at or close to the Fermi level. Furthermore, the low-energy electrons should come only from the Dirac nodes, *i.e.* there should be no other Fermi surfaces from other overlapping bands. Young *et al.* proposed  $\beta$ -cristobalite  $\text{BiO}_2$  as a symmetry-enforced Dirac semimetal (4) that satisfies these criteria. The crystal structure of  $\beta$ -cristobalite  $\text{BiO}_2$  in space group **277** ( $Fd\bar{3}m$ ) is shown in Fig. 1(a). It is isostructural to  $\beta$ -cristobalite  $\text{SiO}_2$  which consists of silicon atoms on a diamond lattice with oxygen atoms placed midway along each silicon-silicon bond. The first-principles band structure of  $\beta$ -cristobalite  $\text{BiO}_2$  in Fig. 1(c) clearly show fourfold-degenerate band crossings with linear dispersion at the X points. The experimental confirmation of the Dirac semimetal phase in  $\text{BiO}_2$  has remained illusive, however, due to its chemical instability. Subsequently, further materials candidates were identified in the distorted spinels, such as  $\text{BiZnSiO}_4$ ,  $\text{BiCaSiO}_4$ ,  $\text{BiAlInO}_4$ , and  $\text{BiMgSiO}_4$  (62), a family of cluster compounds  $\text{AMo}_3\text{X}_3$  with  $A = (\text{Na}, \text{K}, \text{Rb}, \text{In}, \text{Tl})$ , and  $X = (\text{Se}, \text{Te})$  and  $\text{HfI}_3$  (54). Despite these predictions, this type of nonsymmorphic Dirac semimetals has not yet been experimentally realized.

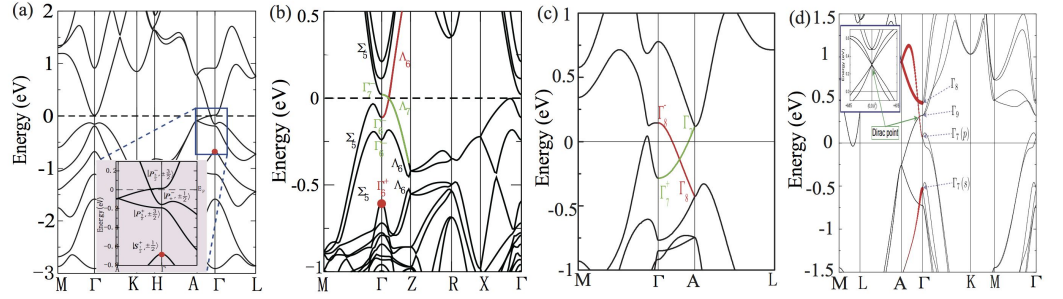


**Figure 2**

**Band inversion induced Dirac semimetal.** Shown are band structures of band inversion induced Dirac semimetals obtained from first-principles calculations. The Dirac points are located on the rotation axis and protected by rotation symmetry. Panels (a) and (b) show the experimentally confirmed Dirac semimetal materials  $\text{Na}_3\text{Bi}$  and  $\text{Cd}_3\text{As}_2$  with space group **194** ( $P6_3/mmc$ ) and **137** ( $P4_2/nmc$ ), respectively. Panels (c) and (d) show the proposed hexagonal  $ABC$  materials  $\text{BaAgBi}$  and  $\text{LiZnBi}$  with nonpolar and polar space groups **194** ( $P6_3/mmc$ ) and **186** ( $P6_3mc$ ), respectively. Adapted from Ref. (5, 63, 64, 65).

The other type of three-dimensional Dirac semimetals, referred to as *topological* Dirac semimetals, arise due to symmetry-protected band crossings induced by a band inversion. While a band inversion generically results in avoided crossings, in the presence of rotation symmetry gap closures can occur when bands with different rotation eigenvalues cross on the rotation axis. On the rotational axis, in the presence of  $\mathcal{T}$  and  $\mathcal{P}$  symmetry, all twofold-degenerate bands can be labeled by representations of rotation axis little group. A crossing of two of these bands with different symmetry representations then leads to stable fourfold-degenerate Dirac points on the rotation axis. Yang and Nagaosa have systematically considered such accidental band crossings and classified the rotation symmetry-protected Dirac semimetals, finding that  $n$ -fold rotations  $C_n$  with  $n = 3, 4, 6$  can stabilize band inversion induced Dirac points (66). The stability of a such a Dirac point can be formally expressed in terms of a topological number constructed from energy band rotation eigenvalues (28). Note that here the stability is of a weaker kind than the aforementioned symmetry-enforced Dirac semimetals, as the band-inversion can be removed by tuning parameters without breaking symmetries.

The first material candidates were predicted by Wang *et al.*, who proposed a family of alkali pnictides  $\text{A}_3\text{Bi}$  ( $\text{A}=\text{Na}, \text{K}, \text{Rb}$ ) (5) and  $\text{Cd}_3\text{As}_2$  (63) as the realizations of *topological* Dirac semimetals. The band structures of  $\text{Na}_3\text{Bi}$  and  $\text{Cd}_3\text{As}_2$  in the presence of spin-orbit coupling are shown in Fig. 2(a) and (b), exhibiting linear crossing on the rotation  $z$  axis. Although  $\text{Na}_3\text{Bi}$  and  $\text{Cd}_3\text{As}_2$  have different space group and composition, the low-energy electronic structure near  $\Gamma$  giving rise to the Dirac points can be understood from the same effective Hamiltonian given by (5, 63)

$$H(\mathbf{k}) = \varepsilon_0(\mathbf{k}) + \begin{pmatrix} M(\mathbf{k}) & Ak_+ & 0 & B^*(\mathbf{k}) \\ Ak_- & -M(\mathbf{k}) & B^*(\mathbf{k}) & 0 \\ 0 & B(\mathbf{k}) & M(\mathbf{k}) & -Ak_- \\ B(\mathbf{k}) & 0 & -Ak_+ & -M(\mathbf{k}) \end{pmatrix}, \quad (2)$$

where  $k_{\pm} = k_x \pm ik_y$  and the functions  $M(\mathbf{k})$  and  $B(\mathbf{k})$  are defined as  $M(\mathbf{k}) = M_0 - M_1 k_z^2 - M_2(k_x^2 + k_y^2)$  and  $B(\mathbf{k}) = Bk_z k_+^2$ . The parameters  $A$ ,  $B$ , and  $M_{0,1,2}$  are material dependent. The band inversion and thus the presence of Dirac points are controlled by  $M(\mathbf{k})$ . In particular, when the parameters  $M_{0,1,2}$  are all positive (or all negative) the bands are inverted and a pair of Dirac points is located at momenta  $k_z$  given by the solutions to the equation  $M(k_z, 0, 0) = 0$ , giving  $k_z = \pm\sqrt{M_0/M_1}$ .

Expanding the Hamiltonian (2) around these points and keeping only the lowest order linear terms, the Dirac Hamiltonian can be readily obtained. Following the first-principles predictions of the Dirac semimetals in  $\text{Na}_3\text{Bi}$  and  $\text{Cd}_3\text{As}_2$ , angle-resolved photoemission spectroscopy experiments have confirmed the existence of Dirac points in these two materials (67, 68), making them the primary object of experimental studies addressing the special electronic and transport properties of three-dimensional Dirac semimetals.

In addition to these materials, a considerable group of materials with the ZrBeSi structure type has been proposed as topological Dirac semimetals (54, 64). Hexagonal ZrBeSi-type compounds have the space group as  $\text{Na}_3\text{Bi}$  and consist of layers of BeSi honeycomb nets separated by the Zr cations. An example is  $\text{BaAgBi}$ , for which the calculated band structure is shown in Fig. 2(c). The physics of the band inversion giving rise to the Dirac points is similar to  $\text{Na}_3\text{Bi}$ . While all these materials are centrosymmetric, the topological Dirac semimetals can also exist in noncentrosymmetric crystals without inversion symmetry. A general analysis of such semimetals was presented by Gao *et al.* (69), who showed that rotation axes with little groups isomorphic to the  $C_{4v}$  and  $C_{6v}$  point groups allow for stable fourfold-degenerate crossings. Material realizations of noncentrosymmetric Dirac semimetals were proposed in a family of hexagonal  $ABC$  materials with LiGaGe-type structure and polar space group 186 ( $P6_3mc$ ). The  $B$  and  $C$  atoms occupy the sites of a Wurtzite structure and  $A$  forms the interstitial site. Examples include  $\text{LiZnBi}$  (65), shown in Fig. 2(d),  $\text{CaAgBi}$  (70), and  $\text{SrHgPb}$  (71). Another noncentrosymmetric Dirac semimetal is  $\text{Cd}_2\text{As}_3$  in space group 110 ( $I4_1cd$ ) which has a different vacancy order than the centrosymmetric  $P4_2/nmc$  phase.

The Dirac equation given by Eq. (1) describes excitations with linear and isotropic dispersion. In the case of free elementary particles, for which the Dirac equation was introduced, this form follows from the requirement of Lorentz invariance. In contrast, the Dirac theory in crystals is not constrained by Lorentz invariance, allowing for a more general form of the Dirac Hamiltonian. This is clear from Eq. (2), for instance, which implies anisotropic Dirac points. More importantly, however, the general classification of Dirac semimetal phases obtained by Yang and Nagaosa, which is based on the dispersion at the Dirac points, demonstrated that the dispersion can be quadratic or cubic, depending on the symmetry quantum numbers of the bands which cross to form the Dirac point (66). Liu and Zunger proposed a class of quasi-one-dimensional transition-metal monochalcogenides compounds  $A^I(\text{MoX}^{VI})_3$  ( $A^I = \text{Na, K, Rb, In, Tl}$ ;  $X^{VI} = \text{S, Se, Te}$ ) as candidates of an ideal cubic Dirac semimetals (72).

## 2.2. Antiferromagnetic Dirac semimetals

The Dirac semimetals considered in the previous subsection are all nonmagnetic preserving  $\mathcal{T}$  symmetry. Recent progress has been achieved in extending the analysis including magnetic systems. The possibility of stable Dirac points in magnetic systems was addressed by Tang *et al.* (73), showing that an antiferromagnetic ordering of spins that preserves  $\mathcal{PT}$  can protect Dirac point. With the combined symmetry, the bands becomes twofold-degenerate at each momentum and a crossing of bands, protected by a crystal symmetry, can give rise to a fourfold-degenerate Dirac point. First-principles calculations predicted magnetic  $\text{CuMnAs}$  as an antiferromagnetic Dirac semimetal (73).

Subsequent work examined the generalization of symmetry-enforced Dirac semimetals to (antiferro-)magnetic systems, both in two (74) and three dimensions (75). In these systems the existence of Dirac points is mandated by the symmetries of the magnetic space group and the symmetry-enforced degeneracies occur at high-symmetry points of the (magnetic) Brillouin zone. Here, an important role is played by an anti-unitary symmetry composed of time-reversal  $\mathcal{T}$  and a half-translation, *i.e.* a translation conjugate to the magnetic order vector. A systematic symmetry-based analysis of band topology in all 1651 magnetic space groups was performed by Watanabe *et*

*al.*, who identified magnetic space groups which, for specific electron filling constraints, necessarily imply a symmetry protected gapless state (76). To date, further materials have been identified, including  $\text{EuCd}_2\text{As}_2$  (77) protected by  $C_3$  rotation symmetry and  $\text{CeSbTe}$  proposed to host Dirac and Weyl states (78).

### 3. WEYL SEMIMETALS

For a basic understanding of the Weyl semimetal it is helpful to return to the Dirac Hamiltonian of Eq. (1). In the massless case, when  $m = 0$ , the Dirac Hamiltonian decouples into two separate equations given by  $\pm v\mathbf{k} \cdot \boldsymbol{\sigma}$ , where each equation describes a two-component chiral Weyl fermion with chirality  $\pm 1$ . In general, a two-component Weyl fermion described by the Weyl equation can arise in solids when two non-degenerate energy bands touch at a point  $\mathbf{k}_0$  in momentum space. Clearly, this cannot occur when Kramers degeneracy holds at every momentum  $\mathbf{k}$ , and therefore  $\mathcal{T}$  and  $\mathcal{P}$  symmetry cannot both be present; at least one of these two symmetries must be broken. In the absence of any crystalline symmetries a linear touching of non-degenerate bands can occur at a generic momentum  $\mathbf{k}_0$  in the three-dimensional Brillouin zone. One may expand the Hamiltonian about the degeneracy point to linear order in momentum  $\delta\mathbf{k} = \mathbf{k} - \mathbf{k}_0$  to obtain

$$H(\delta\mathbf{k}) = \varepsilon_0(\mathbf{k}_0) + \mathbf{v}_0 \cdot \delta\mathbf{k} + \sum_{i,j=x,y,z} v_{ij} \delta k_i \sigma_j, \quad (3)$$

where  $\sigma_{x,y,z}$  are again the Pauli matrices and  $\mathbf{v}_0, \mathbf{v}_{x,y,z}$  characterize the band dispersion near the touching point. The significance of the second terms in (3) will be discussed in Section 3.2, here we focus attention on the third term, which encodes the topological structure of the Weyl point.

To see this, let us first note that when  $v_{ij} = v\delta_{ij}$  one recovers  $v\delta\mathbf{k} \cdot \boldsymbol{\sigma}$ , indicating that (3) indeed describes a Weyl fermion. The topology of Weyl fermions follows from the fact that Weyl points are monopoles of momentum space Berry curvature. The Berry curvature  $F_n^{ab}(\mathbf{k})$  of a particular energy band labeled by  $n$  is the field strength of the Berry connection  $\mathcal{A}_n^a(\mathbf{k})$  and is defined as

$$\mathcal{F}_n^{ab}(\mathbf{k}) = \nabla^a \mathcal{A}_n^b(\mathbf{k}) - \nabla^b \mathcal{A}_n^a(\mathbf{k}), \quad \mathcal{A}_n^a(\mathbf{k}) = -i\langle \psi_n(\mathbf{k}) | \nabla^a | \psi_n(\mathbf{k}) \rangle, \quad (4)$$

where  $\nabla^a \equiv \partial/\partial k_a$  and  $a, b = x, y, z$ . Defining the momentum space ‘‘magnetic field’’ as  $\mathcal{B}_n^a(\mathbf{k}) = \epsilon_{abc} \mathcal{F}_n^{bc}(\mathbf{k})/2$  the topological nature of a Weyl point at momentum  $\mathbf{k}_0$  can be expressed as the quantized monopole density  $\frac{1}{2\pi} \nabla \cdot \mathcal{B}_n(\mathbf{k}) = q\delta(\mathbf{k} - \mathbf{k}_0)$ . For the general Weyl Hamiltonian given by (3) one finds  $q = \text{sgn}(\text{Det } v_{ij})$ . In the particular case  $H(\delta\mathbf{k}) = \pm v\delta\mathbf{k} \cdot \boldsymbol{\sigma}$  this reduces to  $q = \pm 1$  and the momentum space magnetic field of the valence band is given by  $\mathcal{B}(\delta\mathbf{k}) = \pm\delta\mathbf{k}/2|\delta\mathbf{k}|^3$ . Integrating  $\mathcal{B}(\delta\mathbf{k})$  over a Fermi surface sheet surrounding the Weyl point defines the Chern number  $C = \int \mathcal{B} \cdot d\boldsymbol{\Omega}/2\pi$  and equals the monopole charge  $C = \pm 1$ . (In general  $C = q$ .)

Two important consequences directly follow from this. First, since the Nielsen-Ninomiya theorem (79) states that the total monopole charge integrated over the Brillouin zone must vanish, the sum over all chiral fermions must be zero (see also Section 5.2). In a system with only chiral Weyl fermions the Weyl points must come in pairs of opposite monopole charge. (This is, for instance, why the massless Dirac equation of Eq. (1) decouples into two Weyl equations with opposite chirality.) Second, since  $\mathcal{T}$  symmetry implies  $\mathcal{F}_n^{ab}(\mathbf{k}) = -\mathcal{F}_n^{ab}(-\mathbf{k})$  and  $\mathcal{P}$  symmetry implies  $\mathcal{F}_n^{ab}(\mathbf{k}) = \mathcal{F}_n^{ab}(-\mathbf{k})$ , the Berry curvature vanishes when both symmetries are present. Hence, the symmetry properties of the Berry curvature provide a more formal argument way of demonstrating that the existence of Weyl points requires at least one of these symmetries to be broken.

The most important implication of these considerations is the topological stability of Weyl points: since monopoles of Berry curvature cannot be removed unless they are brought to coincidence with monopoles of opposite charge, Weyl points are topologically stable as long as they remain



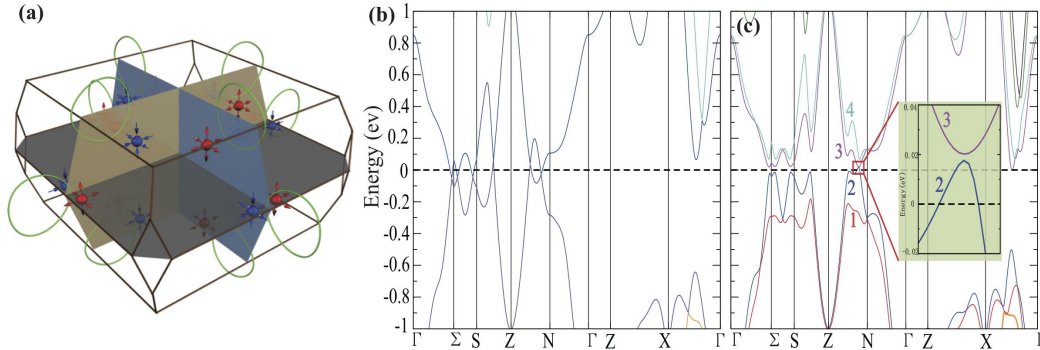


**Figure 3**

**Weyl semimetal.** Panel (a) shows a three-dimensional view of the Weyl points in TaAs, indicated by red and blue dots. The colors and arrows represent the monopole charge of the Weyl points. The green rings represent the nodal rings which are present in the band structure when spin-orbit coupling is not taken into account. Panels (b) and (c) show the calculated band structures of TaAs without and with including the spin-orbit coupling, respectively. Note that the Weyl points of TaAs exist off the high-symmetry lines and are not apparent from (c). Adapted from Ref. (7).

separated in momentum space. In particular, a topological phase transition from a Weyl semimetal phase to an insulating phase requires tuning Hamiltonian parameters to bring pairs of Weyl points together, allowing them to hybridize and annihilate; the degeneracy of a single Weyl point cannot be removed. A more heuristic (and perhaps more intuitive) way to state this result is to say that for the Weyl Hamiltonian  $H(\delta\mathbf{k}) = v\delta\mathbf{k} \cdot \boldsymbol{\sigma}$ , or its more general version  $H(\delta\mathbf{k}) = \sum_{ij} v_{ij}\delta k_i \cdot \sigma_j$ , it is not possible to write down a mass term, since all Pauli matrices have been already been used.

### 3.1. Realizations of $\mathcal{T}$ -broken and $\mathcal{P}$ -broken Weyl semimetals

As discussed above, the Weyl semimetal phase relies on breaking either  $\mathcal{T}$  or  $\mathcal{P}$  symmetry (or possibly both). This has inspired two broad categories of proposals for realizing Weyl semimetals. The first category comprises magnetic candidate materials, which includes the first proposal for a Weyl semimetal by Wan *et al.* (6). Wan *et al.* considered a class of magnetic pyrochlores  $A_2\text{Ir}_2\text{O}_7$ , where  $A$  is Y or rare earth element Eu, Nd, Sm, or Pr, and predicted based on first-principles calculations that an "all-in, all-out" noncollinear magnetic order gives rise to Weyl points. In addition to the magnetic pyrochlores, the ferromagnetic half-metal  $\text{HgCr}_2\text{Se}_4$  was predicted to host Weyl points (80). More recently, a class of magnetic Co-based magnetic Heusler compounds has been proposed as Weyl semimetals (81, 82), in addition to the antiferromagnetic  $\text{Mn}_3\text{Sn}$  family of materials (83) and layered half-metal  $\text{Co}_3\text{Sn}_2\text{S}_2$  (84). These magnetic Weyl semimetals exhibit giant anomalous Hall effect in experiment (85, 86, 87, 88), which provides strong evidence for the existence of Weyl points. Another route to the realization of  $\mathcal{T}$ -breaking Weyl semimetal is based on splitting the two Weyl nodes which form Dirac point, see Eq. (1). To achieve this, Burkov and Balents proposed a heterostructure of alternating layers of magnetically doped topological insulator and normal insulator (89). A similar proposal is based on an CdO/EuO superlattice, in which case ferromagnetically ordered EuO is the normal insulator (90).

The second category of proposals for Weyl semimetal phases is focused on noncentrosymmetric systems with strong spin-orbit coupling. Compared to magnetic materials, nonmagnetic Weyl semimetals have the advantage that the electronic structure is more easily probed by angle-resolved photoemission spectroscopy. Inversion symmetry breaking Weyl semimetals differ from  $\mathcal{T}$  breaking

Weyl semimetals by the minimum number of Weyl points present in the band structure. This can be understood from the effect of  $\mathcal{T}$  symmetry: a Weyl point at  $\mathbf{k}_0$  must have a partner at  $-\mathbf{k}_0$  with the same chirality. Since the sum of chiralities of all Weyl points must be zero, this implies the existence of two more Weyl points and leads a minimal number of four Weyl points (assuming other types of chiral fermions are absent, see Section 5).

Different routes were explored to realize the  $\mathcal{T}$ -invariant Weyl semimetal phase. One route made use of Murakami's theory of the phase transition between the topological insulator and normal insulator in noncentrosymmetric materials, as such phase transition must necessarily occur via an intermediate Weyl semimetal phase (50). An example of such proposal is the solid solution  $\text{LaBi}_{1-x}\text{Sb}_x\text{Te}_3$  of the topological insulator  $\text{LaBiTe}_3$  and normal insulator  $\text{LaSbTe}_3$  (91). Another route, which is not unrelated to the former, has led to proposals based on the heterostructure principle, where layers of topological insulator and normal insulator are stacked to form a superlattice (10, 92, 93). There is, however, no experimental realization of the above proposals so far.

A decisive advance came in 2015, when the observation of a  $\mathcal{T}$ -invariant Weyl semimetal phase was reported in TaAs and related materials (94, 95, 96, 97, 98, 99) based on earlier theoretical predictions (7, 33). The band structure of TaAs is shown in Fig. 3. The experimental discovery of Weyl fermions in TaAs cemented the field of TSMS and fueled the subsequent quest for new Weyl and other semimetal phases.

Ideal Weyl semimetals should have the following properties: (i) the Weyl points sit at the Fermi energy; (ii) there are no other band structure features, such electron or hole pockets, overlapping in energy; and (iii) the Weyl points have a relatively large separation in momentum space. A Weyl semimetal satisfying criteria (i) and (ii) was proposed in the strained HgTe material class and in a  $\text{CuTlTe}_2$  family of materials (100). A large separation of Weyl points is useful for experimental detection of the surface Fermi arc states and in this sense  $\text{WP}_2$  and  $\text{MoP}_2$  (101), as well as  $\text{Ta}_3\text{S}_2$  (102) and  $\text{CuTlTe}_2$  are promising candidates. For experimental studies it is furthermore desirable to have a system with a small number of Weyl points and with this in mind material candidates hosting the minimum number of four Weyl points were proposed, notably including the ternary compound  $\text{TaIrTe}_4$  (103) and  $\text{MoTe}_2$  (104).

In the introductory discussion of this section we have mentioned that Weyl points may be annihilated by merging two partners with opposite chirality. This is enabled by the fact that a twofold band touching can occur at generic momenta in the Brillouin zone and is not necessarily pinned to one particular point. It is, however, possible for a (single) Weyl point to occur at a  $\mathcal{T}$  invariant momentum. Kramers degeneracy then pins the Weyl fermion to the  $\mathcal{T}$  invariant momentum, leading to an irremovable Weyl point. Such Weyl points are referred to as Kramers-Weyl fermions and can only occur in the 65 chiral space groups which lack inversion, mirror, and any other roto-inversion symmetries (105). Several material candidates were proposed, including  $\text{Ag}_2\text{Te}$  and  $\text{Ag}_3\text{BO}_3$  (105).

The breaking of  $\mathcal{P}$  symmetry in nonmagnetic Weyl semimetals suggests that they may have interesting nonlinear optical properties, such as second harmonic generation and shift current, and these nonlinear optical responses have recently attracted much recent attention (106, 107, 108, 109, 110, 111). In particular, this attention has focused on the contribution of the Weyl fermions to the nonlinear optical response. Remarkably, the Weyl semimetal systems TaAs, TaP, and NbAs were found to have the largest the largest second harmonic generation ever recorded (108).

### 3.2. Type-II and multi-Weyl semimetals

Let us now return to Eq. (3) describing the general form of the Hamiltonian near a Weyl point. We have shown that the third term encodes the topological property of the Weyl point (*i.e.* the

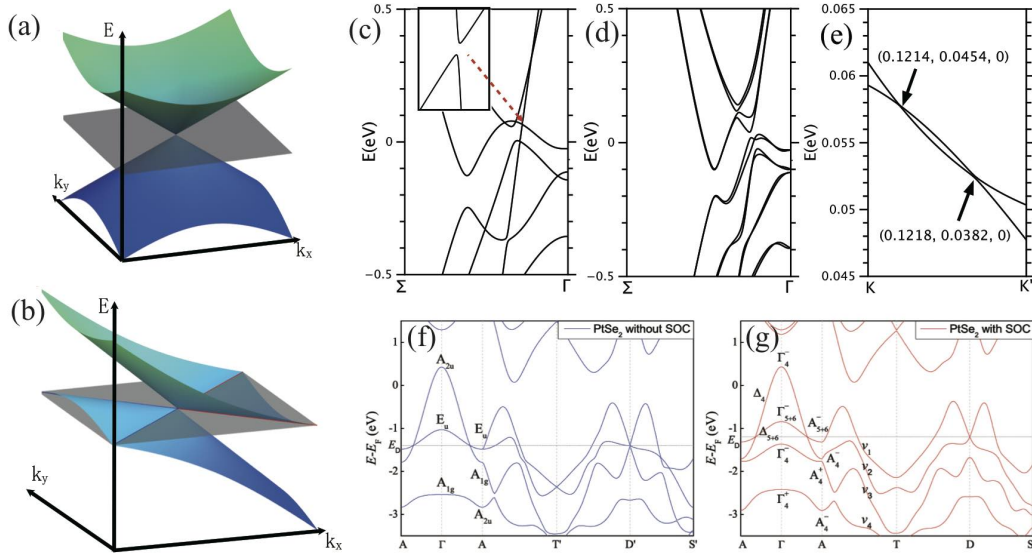


**Figure 4**

**Type-II topological semimetals.** Panels (a) and (b) show the energy dispersion and Fermi surface of Type-I and Type-II Weyl/Dirac semimetals, respectively. Type-I Weyl/Dirac point with a point-like Fermi surface. A type-II Weyl/Dirac point appears as the contact point between electron and hole pockets. The grey plane corresponds to the position of the Fermi level, and the blue (red) lines mark the boundaries of the hole (electron) pockets. Panels (c) and (d) show the band structures of  $\text{WTe}_2$  without and with SOC. Panel (e) shows one of the four pairs of Weyl points in  $\text{WTe}_2$ . Panels (f) and (g) show the band structures of  $\text{PtSe}_2$  without and with spin-orbit coupling. *Adapted from Refs. (11, 112)*

monopole charge) and in the simplest case takes the form an isotropic Weyl fermion. The second term, given by  $\mathbf{v}_0 \cdot \delta \mathbf{k}$ , is important for the dispersion of the Weyl points and gives rise to a qualitative distinction between two types of Weyl points, called type-I and type-II Weyl points (11). The phases which host these Weyl points are referred to as type-I and type-II Weyl semimetals. To understand this distinction, consider the energy spectrum corresponding to Eq. (3) given by the two branches (ignoring the constant contribution)

$$\varepsilon_{\pm}(\delta \mathbf{k}) = \mathbf{v}_0 \cdot \delta \mathbf{k} \pm \sqrt{\sum_{i,j=x,y,z} \delta k_i (v v^T)_{ij} \delta k_j} \equiv T(\delta \mathbf{k}) \pm U(\delta \mathbf{k}). \quad (5)$$

Here,  $T(\delta \mathbf{k})$  and  $U(\delta \mathbf{k})$  may be viewed as the kinetic and potential part of the energy spectrum. Weyl points of type-II are then defined by the condition that for some direction  $\delta \hat{\mathbf{k}} = \delta \mathbf{k} / |\delta \mathbf{k}|$  in momentum space the kinetic energy exceeds the potential energy:  $T(\delta \hat{\mathbf{k}}) > U(\delta \hat{\mathbf{k}})$ . This is associated with a qualitatively different structure of the spectrum, as it necessarily implies open electron and hole pockets when the Fermi energy is at the Weyl point. Instead, the Fermi surfaces of type-I Weyl points are closed and consist of a single point when the Fermi level is at the band crossing point. This is illustrated in Figs. 4 (a) and (b), which show a type-I and type-II Weyl point, respectively. An intuitive way to picture this difference is to view a type-II Weyl point as a Weyl fermion with an over-tilted cone. Clearly, the tilting of the cone is due to the vector  $\mathbf{v}_0$  in Eq. (3) and can thus be called a tilt-vector.

The Weyl points observed in the TaAs material class are examples of type-I fermions. Soluyanov *et al.*, who pointed out the existence of these two distinct types of Weyl fermions, proposed  $\text{WTe}_2$

as a possible material candidate to host Weyl points of type-II. The electronic band structure (in the presence of spin-orbit coupling) is reproduced in Fig. 4 (d) and Fig. 4 (e) shows the crossing of energy bands defining type-II Weyl points. Following this proposal, more material candidates were identified based on first-principles calculations, including  $\text{MoTe}_2$  (104), the  $\text{WP}_2$  material family (101),  $\text{TaIrTe}_4$  (103),  $\text{Ta}_3\text{S}_2$  (102), and  $\text{LaAlGe}$  (113).

Given the intimate relation between Weyl and Dirac fermions it is not surprising that the classification of Weyl fermions into type-I and type-II can also be applied to Dirac semimetals. From this perspective, the experimentally observed Dirac semimetals  $\text{Na}_3\text{Bi}$  and  $\text{Cd}_3\text{As}_2$  mentioned in Section 2.1 realize type-I Dirac fermions, as may be checked from Eq. (2). The realization of a Type-II Dirac semimetal was predicted in the family of transition-metal icosagenides  $\text{MA}_3$  with  $M = (\text{V}, \text{Nb}, \text{Ta})$  and  $A = (\text{Al}, \text{Ga}, \text{In})$  (114) and in the  $\text{PtTe}_2$  material family (112). The band structure of  $\text{PtTe}_2$  exhibiting type-II Dirac points is shown in Fig. 4 (g).

The distinction between type-I and type-II Weyl fermions only arises in the context of condensed matter realizations of Weyl fermions. As alluded to in Section 2, this is due to the lack of Lorentz invariance in condensed matter systems and leads to an additional categorization of Weyl points based on their dispersion. As shown by Fang *et al.* (115), apart from linear dispersion, Weyl fermions realized in crystals can have quadratic or cubic dispersion, depending on the rotation eigenvalues of the band which cross at the Weyl point. Notably, such “multi-Weyl” points have a monopole charge  $q$  larger than that of the ordinary linear Weyl fermion. In particular, Weyl points with quadratic and cubic dispersion have monopole charge  $q = \pm 2$  and  $q = \pm 3$ , respectively. The proposed ferromagnetic Weyl semimetal  $\text{HgCr}_2\text{Se}_4$  (80) is an example of a “multi-Weyl” semimetal, hosting Weyl points with quadratic dispersion. In addition,  $\text{SrSi}_2$  was proposed as a charge  $q = \pm 2$  Weyl semimetal (116).

## 4. NODAL LINE SEMIMETALS

In this section, we review another class of topological semimetals referred to as topological nodal line semimetals. Nodal line semimetals feature gapless excitations along one-dimensional nodal lines formed from the linearly touching conduction and valence bands (8, 9, 10). Nodal line degeneracies protected by crystalline symmetries can generically occur when bands with different crystal symmetry eigenvalues cross along a rotational axis or on a mirror- or glide-invariant plane of the BZ. In contrast to this type of nodal lines, nodal lines can occur due to band topology, in which case they are associated with a topological invariant.

A variety of topological nodal line semimetal classes have been identified, which can be distinguished based on characteristics such as topological invariants (117), degeneracy of the band crossing (69), Fermi surface geometry (118, 119), and the linking structure of multiple nodal lines (120). In this section, we review the characteristic features and material realizations of representative examples, which include  $\mathbb{Z}_2$  Berry phase nodal line semimetals,  $\mathbb{Z}_2$  monopole nodal line semimetals, and  $\mathbb{Z}$  mirror- or glide-symmetric nodal lines. More comprehensive reviews of nodal line semimetals can be found in Refs. (42, 31).

### 4.1. $\mathbb{Z}_2$ Berry phase nodal line semimetals

This class of nodal line semimetals hosts fourfold-degenerate Dirac nodal lines (including spin degree of freedom) in momentum space characterized by the  $\mathbb{Z}_2$  quantized Berry phase. In the limit of vanishing spin-orbit coupling, assuming both time-reversal  $\mathcal{T}$  and inversion  $\mathcal{P}$  symmetry are present, the (doubly) Kramers degenerate bands can cross without opening a band gap along a one-dimensional line; this crossing is protected by a nontrivial  $\mathbb{Z}_2$  quantized Berry phase, resulting in the formation of a fourfold-degenerate Dirac nodal line (121). The  $\mathbb{Z}_2$  Berry phase can be readily

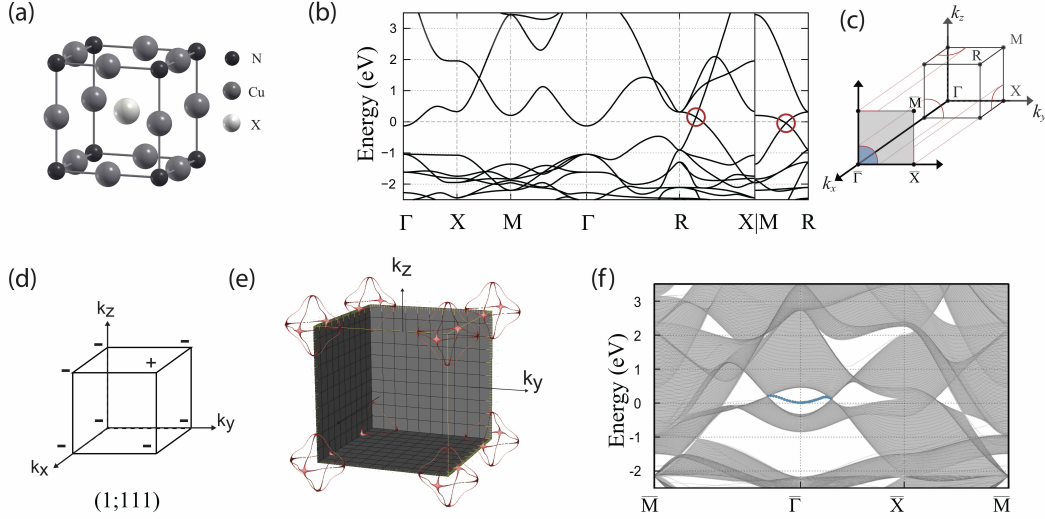


**Figure 5**

**Nodal line semimetal in  $\text{Cu}_3\text{NX}$ .** (a) Anti-perovskite structure of  $\text{Cu}_3\text{NX}$ , where  $X = \text{Pd}$  or  $\text{Zn}$ . (b) Band structure of  $\text{Cu}_3\text{NPd}$ . The crossing points indicated by red circles correspond to the points that comprise a Dirac nodal line. (c) Bulk and surface BZs. (d) Parity eigenvalues evaluated at eight time-reversal invariant points of  $\text{Cu}_3\text{NZn}$ . (e) Nodal lines of  $\text{Cu}_3\text{NPd}$  in momentum space. (f) Surface energy spectrum of  $\text{Cu}_3\text{NZn}$ . Adapted from Ref. (121)

evaluated from the parity eigenvalues of all the occupied Bloch states at the time-reversal invariant momenta. The Berry phase  $\Omega(C_{abcd})$  corresponding to a closed loop  $C_{abcd}$  which visits four time-reversal invariant momenta (TRIMs)  $\Gamma_{a,b,c,d}$  is represented in terms of the parity eigenvalues as  $\Omega(C_{abcd}) = \log(\xi_a \xi_b \xi_c \xi_d)/i$ . Here,  $\xi_a = \prod_n \xi_n(\Gamma_a) = \pm 1$  are the parity eigenvalues of the occupied Bloch states at the eight time-reversal invariant momenta  $\Gamma_a$ , where  $a = 1, \dots, 8$ . When  $\Omega(C_{abcd}) = \log(-1)/i = \pi$ , an odd number of Dirac nodal lines must pierce any interior surface  $S_{abcd}$  that has the time-reversal invariant path  $C_{abcd}$  as its boundary. The  $\mathbb{Z}_2$  Berry phases defined in terms of the parity eigenvalues, and corresponding to different surfaces  $S_{abcd}$ , are quite similar to the (strong and weak) topological indices  $(\nu_0; \nu_1 \nu_2 \nu_3)$  characterizing topological insulators in three dimensions (122, 123). We comment on this connection in more detail below. The  $\mathbb{Z}_2$  invariant of Dirac nodal line semimetals given by the Berry phase formula can also be understood as the topological invariant characterizing one-parameter families of Hamiltonians in class AI (124).

The representation of the  $\mathbb{Z}_2$  Berry phase in terms of the band parity eigenvalues establishes an interesting link between the nodal line semimetals and the time-reversal invariant topological insulators with strong spin-orbit interaction. Indeed, in centrosymmetric topological insulators the  $\mathbb{Z}_2$  topological indices can similarly be represented in terms of the parity eigenvalues  $\xi_a$  (123). In both cases the topological indices constructed from the parity eigenvalues signal the presence of a band inversion. As a result, a  $\mathbb{Z}_2$  Berry phase Dirac nodal line semimetal is turned into a  $\mathbb{Z}_2$  topological insulator when spin-orbit coupling is activated, provided spin-orbit coupling does not undo the band inversion at a TRIM, thus changing the parity eigenvalues of the occupied Bloch states.

Apart from establishing a conceptual connection to  $\mathbb{Z}_2$  topological insulating phases, the representation of  $\mathbb{Z}_2$  Berry phase in terms of parity eigenvalues also provides important insight into ways to realize nodal line semimetals in real materials. When bands are inverted such that the

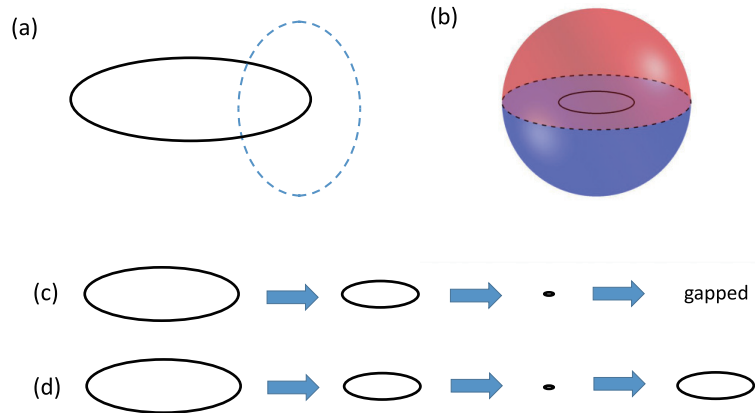


**Figure 6**

**$\mathbb{Z}_2$  Berry phase.** (a) A nontrivial  $\mathbb{Z}_2$  Berry phase of  $\pi$  calculated on a loop in 3D BZ (dashed blue line) implies the presence of a nodal line (solid black line) passing through the loop. (b) A nontrivial  $\mathbb{Z}_2$  monopole charge calculated on a 2D sphere implies the presence of a nodal line enclosed by the sphere. (c) Nodal line with nontrivial Berry phase  $\pi$  and the zero monopole charge. It can be created (annihilated) alone as the bands are inverted (uninverted). (d) Nodal line with both nontrivial Berry phase and the nonzero monopole charge. It can be reduced to a Dirac point but cannot be annihilated, but reverted into a nodal line. *Adapted from Ref. (117)*

parity eigenvalues change at a TRIM, the band inversion guarantees the presence of the nodal line. Furthermore, when the band inversion could be tuned via impurity doping or strain (121, 125, 126), the size of the nodal line can be engineered, providing a potential route to realize strongly-correlated nearly-flat bands localized on the surface (121, 127, 128). This insight has guided the proposal of  $\text{Cu}_3\text{NX}_x$  as a promising candidate for the Dirac line node semimetal, where  $X = \text{Pd}$  or  $\text{Zn}$ , and  $x$  is a doping rate of the  $X$  atom. It was found that doping a transition metal  $X$  induces band inversion in  $\text{Cu}_3\text{N}$  without opening a band gap, giving rise to a Dirac line node. Independently,  $\text{Cu}_3\text{NZn}$  was proposed to be the topological nodal line semimetal by Rui Yu *et al.* (129). A large number of materials have been theoretically identified in this class of the nodal line semimetals, with the experimental realizations in graphite (130, 131), ZrSiS family (132, 36, 133, 134, 135) and  $\text{TiB}_2$  family (136, 137),  $\text{Mg}_3\text{Bi}_2$  (138).

## 4.2. $\mathbb{Z}_2$ monopole nodal line semimetals

In addition to the  $\mathbb{Z}_2$  Berry phase, which characterizes a one-parameter family of Hamiltonians in 3D momentum space, a nodal line can also carry a  $\mathbb{Z}_2$ -quantized monopole charge when both  $\mathcal{P}$  and  $\mathcal{T}$  are present and spin-orbit coupling is vanishingly small. The  $\mathbb{Z}_2$  monopole charge characterizes a two-parameter family of Hamiltonians in 3D momentum space (117, 139, 140). Unlike the nodal lines protected by the Berry phase, the nodal lines with a nontrivial monopole charge are stable in the sense that they can only be removed by pairwise annihilation; an isolated monopole charge nodal line cannot be removed. This is similar to Weyl points discussed in Section 3 and is illustrated in Fig. 6. Here, the  $\mathbb{Z}_2$  monopole charge originates from the nontrivial second homotopy group of the classifying space of *real* Bloch states (141, 142, 117), in contrast with the integer monopole charge of *complex* Weyl fermions in systems with strong spin-orbit coupling.

More specifically, the  $\mathbb{Z}_2$  monopole charge manifests itself as a linking number which can be

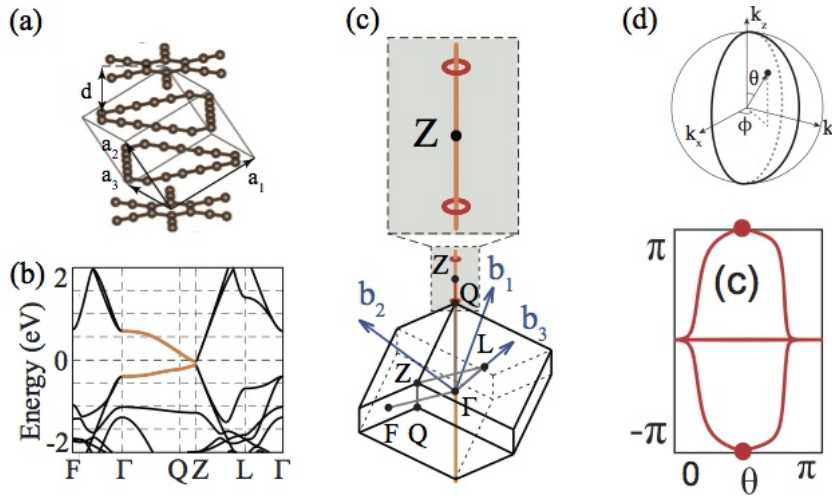


**Figure 7**

**$\mathbb{Z}_2$  monopole nodal line semimetal.** DFT prediction for the  $\mathbb{Z}_2$  monopole nodal line semimetal in an ABC stack of 2D graphdiyne. (a) Atomic structure, (b) electronic band structure. Orange lines indicate nodal lines formed between the two highest occupied bands and the two lowest unoccupied bands. (c)  $\mathbb{Z}_2$  nodal lines in the BZ. Red nodal lines are the  $\mathbb{Z}_2$  monopole nodal lines, and the orange nodal line indicates the nodal line formed from the two highest occupied bands. (d) Wilson bands calculated on the sphere parameterized by polar coordinates shown in the top panel. Adapted from (143)

evaluated from the electronic band structure (143). Ahn *et al.* (143) have proved that the  $\mathbb{Z}_2$  monopole charge is given by the linking number  $\text{Lk}(\gamma, \tilde{\gamma}_j) = \frac{1}{4\pi} \oint_{\gamma} d\mathbf{k} \times \oint_{\tilde{\gamma}_j} d\mathbf{p} \cdot \frac{\mathbf{k}-\mathbf{p}}{|\mathbf{k}-\mathbf{p}|^3}$ , where  $\gamma$  ( $\tilde{\gamma}_j$ ) represents the nodal line formed from the conduction and valence (two top-most occupied bands). Furthermore, the  $\mathbb{Z}_2$  monopole charge carried by a red nodal line can be represented by the second Stiefel-Whitney number  $w_2$  defined as

$$w_2 = \sum_{\tilde{\gamma}_j} \text{Lk}(\gamma, \tilde{\gamma}_j), \quad (6)$$

which can be evaluated by the Wilson band calculations on a sphere enclosing the nodal line. Recently, the nodal line semimetal characterized by the  $\mathbb{Z}_2$  monopole charge was identified in ABC-stacked graphdiyne shown in Fig. 7(a) (144, 143). The Brillouin zone contains two nodal lines in the vicinity of the Z point, which are linked by another nodal line formed between the highest occupied bands colored by orange in Figs. 7 (b) and (c). The corresponding linking number calculation gives a linking number of 1. The  $\mathbb{Z}_2$  monopole charge is consistent with the linking number, which is evaluated from the Wilson bands on the sphere enclosing a nodal line, shown in Fig. 7 (d).

### 4.3. Mirror- and glide mirror-symmetry protected nodal line semimetals

Crystals preserving a mirror ( $\mathcal{M}$ ) or a glide-mirror ( $\mathcal{G}$ ) symmetry can also host nodal lines on a mirror (glide)-invariant plane in momentum space. The bands with different mirror (glide-mirror) eigenvalues can cross without hybridizing on the two-dimensional invariant plane, resulting in degeneracies along one-dimensional lines. This mirror-protected nodal line is topological and carries a  $\mathbb{Z}$  topological invariant  $\zeta$  defined by

$$\zeta = \frac{N_A - N_B}{2}, \quad (7)$$

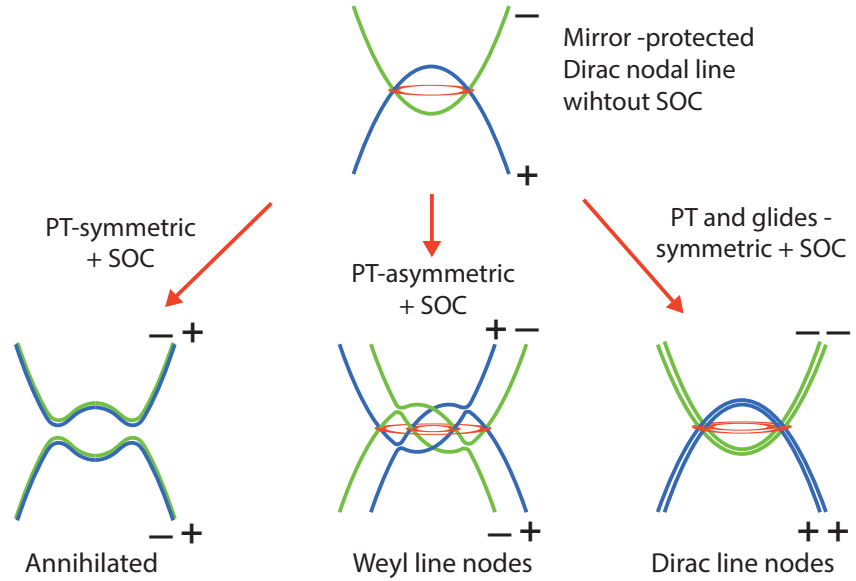


**Figure 8**

**Mirror protected nodal line semimetal.** Schematic illustration of possible band evolution of mirror protected nodal line due to spin-orbit coupling. The mirror  $-$  and  $+$  bands are colored by green and blue, respectively.

where  $N_A$  ( $N_B$ ) is the number of occupied bands with mirror eigenvalue  $+$  at two different points  $A$  and  $B$  on the mirror invariant plane.  $|\zeta|$  dictates the number of nodal lines intersecting any line connecting the two points. In the absence of spin-orbit coupling a mirror-protected nodal line can be created by a band inversion of bands with distinct mirror eigenvalues. A line node of this kind constitutes an accidental band crossing and does not require a partner as in the case of  $\mathbb{Z}_2$  monopole charge line nodes. Various materials in this class of topological semimetal have been theoretically identified, including the experimentally confirmed materials, such as CaAgP (145, 146, 147) and PbTaSe<sub>2</sub> (148, 149, 150, 147) families of materials.

In the presence of strong spin-orbit coupling, the mirror-protected nodal lines can be either annihilated or split into two twofold-degenerate Weyl line nodes—a fate which is determined by the existence of the combined symmetry  $\mathcal{PT}$ , as shown in Fig. 8. When  $\mathcal{PT}$  is preserved, the Kramers pair  $\psi$  and  $\mathcal{PT}\psi$  should have opposite eigenvalues of the mirror operator. For example, suppose  $\psi_{\pm}$  is an eigenstate of  $M_z$  and thus satisfies  $M_z\psi_{\pm} = \pm i\psi_{\pm}$ . One then has  $M_z\mathcal{PT}\psi_{+} = \mathcal{PT}M_z\psi_{+} = \mathcal{PT}(+i\psi_{+}) = -i\mathcal{PT}\psi_{+}$ , which implies that  $\mathcal{PT}\psi_{+} \sim \psi_{-}$ . Therefore, the twofold-degenerate Bloch states  $\psi_{n\mathbf{k}}$  and  $\mathcal{PT}\psi_{n\mathbf{k}}$  form a Kramers pair with the opposite mirror eigenvalues. As a result, in the presence of spin-orbit coupling the energy bands forming the line node on the mirror invariant plane are allowed to hybridize and will anticross. This is shown in Fig. 8. In contrast, when either  $\mathcal{P}$  or  $\mathcal{T}$  is broken so that the Kramers pair is non-degenerate in energy, the bands with distinct mirror eigenvalues can cross each other forming a twofold-degenerate Weyl nodal line. Thus, the Dirac nodal line that appeared in the absence of spin-orbit coupling is split into two twofold-degenerate nodal lines when spin-orbit coupling is included in this  $\mathcal{PT}$ -asymmetric case. Unlike the mirror-protected nodal lines, the nodal lines protected by nonsymmorphic space group symmetries, such as a glide-mirror or a screw, can survive even in the presence of spin-orbit coupling, retaining the fourfold-degenerate Dirac nodal lines (117, 151). An orthorhombic perovskite iridate, such as



Al<sub>2</sub>O<sub>3</sub>, has been identified to host Dirac nodal line at the boundary of the BZ, protected by a screw and  $\mathcal{PT}$  (152).

## 5. NEW FAMILIES OF TOPOLOGICAL SEMIMETALS

In the previous sections we have focused on TSMs defined by twofold- or fourfold-degenerate band touchings at isolated points or on lines in the Brillouin zone. In particular, we have discussed semimetallic systems which can be described by, or understood from, variations of the Dirac or Weyl equation. In this section, we turn to a discussion of more general classes of TSMs and focus on two classes in particular: stable symmetry-enforced band crossing points which cannot be described by Dirac or Weyl fermions, and “triple-point” fermion semimetals characterized by a symmetry-protected accidental crossing of three bands.

### 5.1. Multifold band crossings in solids and low-energy fermions

As discussed in Section 2, symmetry-enforced Dirac semimetals are defined by fourfold-degenerate band crossings located at high-symmetry points, with linear dispersion and vanishing Chern number. In solids with strong spin-orbit coupling and  $\mathcal{T}$  symmetry, however, more general symmetry-enforced band crossings at points of high symmetry can occur, at which three, six, or even eight bands touch. The conditions for the existence of such nodal band degeneracies are determined by the structure of the crystal space group, which is required to include nonsymmorphic symmetry elements (13). The latter requirement implies that symmetry-protected degeneracy points of this kind are located at high-symmetry points on the BZ boundary. Note that when spin-orbit coupling is vanishingly small, threefold band crossings can also occur for symmorphic space groups (153).

The presence of three-, six-, or eightfold band crossings gives rise to low-energy fermionic excitations which cannot be described by the Dirac or Weyl equations; instead, their dispersion is described by a more general Hamiltonian. The departure from the (low-energy) description of familiar relativistic free fermions (*i.e.* Dirac and Weyl fermions) is a consequence of the less restrictive nature of the crystal symmetries governing condensed matter systems, which allow for the realization of generalized low-energy fermions. All of these TSMs characterized by “multifold” fermions (*i.e.* three-, six-, and eightfold) are symmetry-enforced semimetals, as they fundamentally rely on the constraints originating from space group symmetry, possibly combined with  $\mathcal{T}$  symmetry.

A first example was discussed by Wieder *et al.* (12), who studied and identified space groups which can protect eightfold-degenerate band crossings with linear dispersion. In particular, two tetragonal space groups, **130** ( $P4/ncc$ ) and **135** ( $P4_2/mbc$ ), were considered in detail, since in these space groups all energy levels at the *A* point must be eightfold degenerate, *i.e.* the *A* point only admits eight-dimensional representations. Owing to the linear dispersion for all momenta  $\delta\mathbf{k} = \mathbf{k} - \mathbf{k}_0$  away from the touching point, such eightfold-degenerate points were referred to as “double-Dirac” points. Based on first-principles calculations, Wieder *et al.* predicted that the known material Bi<sub>2</sub>AuO<sub>5</sub> in space group **130** hosts a double-Dirac at the *A* point, which sits close to the Fermi level (12). The calculated band structure for Bi<sub>2</sub>AuO<sub>5</sub> is shown in Fig. 9 (a).

In subsequent work, Bradlyn *et al.* have considered the occurrence of space group symmetry-enforced multifold band crossings from a more general and comprehensive perspective (13). In particular, they exhaustively tabulated all space groups which, in combination with  $\mathcal{T}$  symmetry, can stabilize three-, six-, or eightfold degenerate fermions, focusing on systems with spin-orbit coupling. Furthermore, the authors determined the general form of the Hamiltonian describing these “unconventional fermions”. A series of material candidates was also proposed, including additional examples of materials in space groups **130** and **135** hosting eightfold fermions, such as the bismuth oxides CuBi<sub>2</sub>O<sub>4</sub> and PdBi<sub>2</sub>O<sub>4</sub> (space group **130**), as well as PdS (space group **135**). In

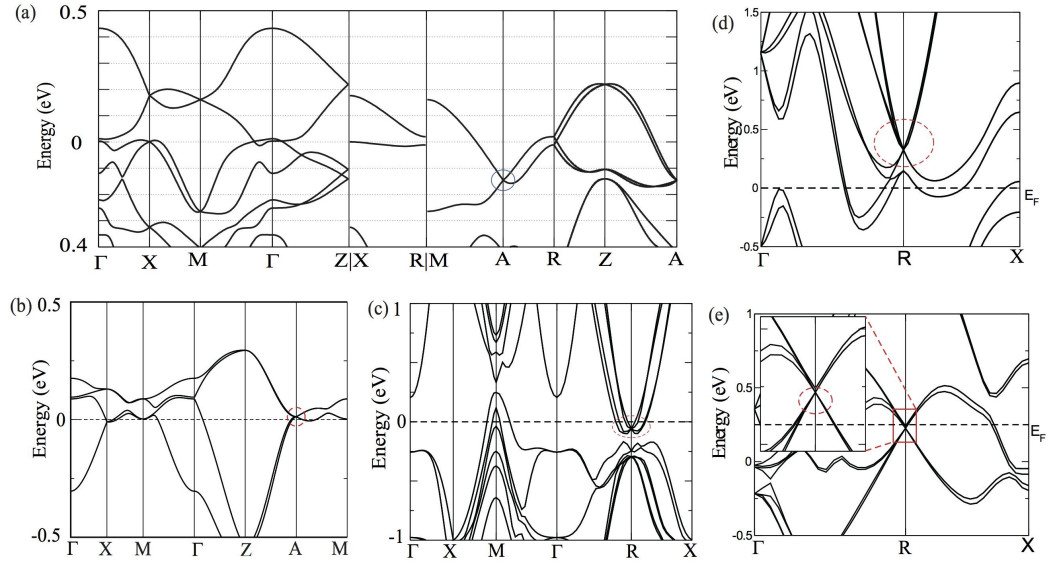


**Figure 9**

**Eightfold and sixfold fermions.** Examples of first-principles band structures showing eightfold and sixfold fermions at points of high symmetry on the Brillouin zone boundary. Eightfold fermions were predicted in (a)  $\text{Ba}_2\text{AuO}_5$ ; (b)  $\text{CuBi}_2\text{O}_4$ ; and (c)  $\text{Ta}_3\text{Sb}$ . Sixfold fermions were predicted in (d)  $\text{MgPt}$  and (e)  $\text{Li}_2\text{Pd}_3\text{B}$ . Adapted from the Refs. (12) and (154)

$\text{CuBi}_2\text{O}_4$ , shown in Fig. 9(b), the eight-band fermion sits at the Fermi level, however, interaction effects may play an important role and render the material insulating (155). The material family  $A_3B$  in space group **223** ( $\text{Pm}\bar{3}\text{n}$ ), where  $A$  is either Nb or Ta and  $B$  is any group A-IV or A-V element in the  $\beta$ -tungsten structure A15, was identified as another candidate for hosting eight-band fermion, as evidenced by  $\text{Ta}_3\text{Sb}$  shown in Fig. 9 (c). Sixfold fermions were predicted in  $\text{MgPt}$  with space group **198** ( $\text{P}2_13$ ), shown in Fig. 9 (d), and in  $\text{Li}_2\text{Pd}_3\text{B}$  **212** ( $\text{P}4_332$ ), shown in Fig. 9 (e), among other examples.

The collection of proposed material candidates is encouraging, yet also showcases one of the remaining challenges for future research. In many examples—for instance those shown in Figure 9—the multifold fermion band crossings do not sit at the Fermi and (or) overlap in energy with generic Fermi surfaces. As a result, isolating the electronic excitations of the multifold fermions in real materials defines the most interesting—and perhaps most pressing—problem to attack in the field of symmetry-enforced semimetals.

## 5.2. Topological fermions with higher spin

The comprehensive classification of space group symmetry-protected band crossings obtained by Bradlyn *et al.* revealed that some of these band crossing points can be described by fermions with spin higher than  $j = 1/2$ . For instance, threefold degenerate point nodes give rise to excitations with spin  $j = 1$ . Such higher spin systems form an interesting class of topological semimetals which deserves further discussion.

Fermions with higher spin can be viewed as generalizations of Weyl fermions. As discussed in Section 3, the Hamiltonian of a Weyl fermion takes the form  $H(\mathbf{k}) = v_0 \delta \mathbf{k} \cdot \boldsymbol{\sigma}$ , where  $\delta \mathbf{k}$  is the

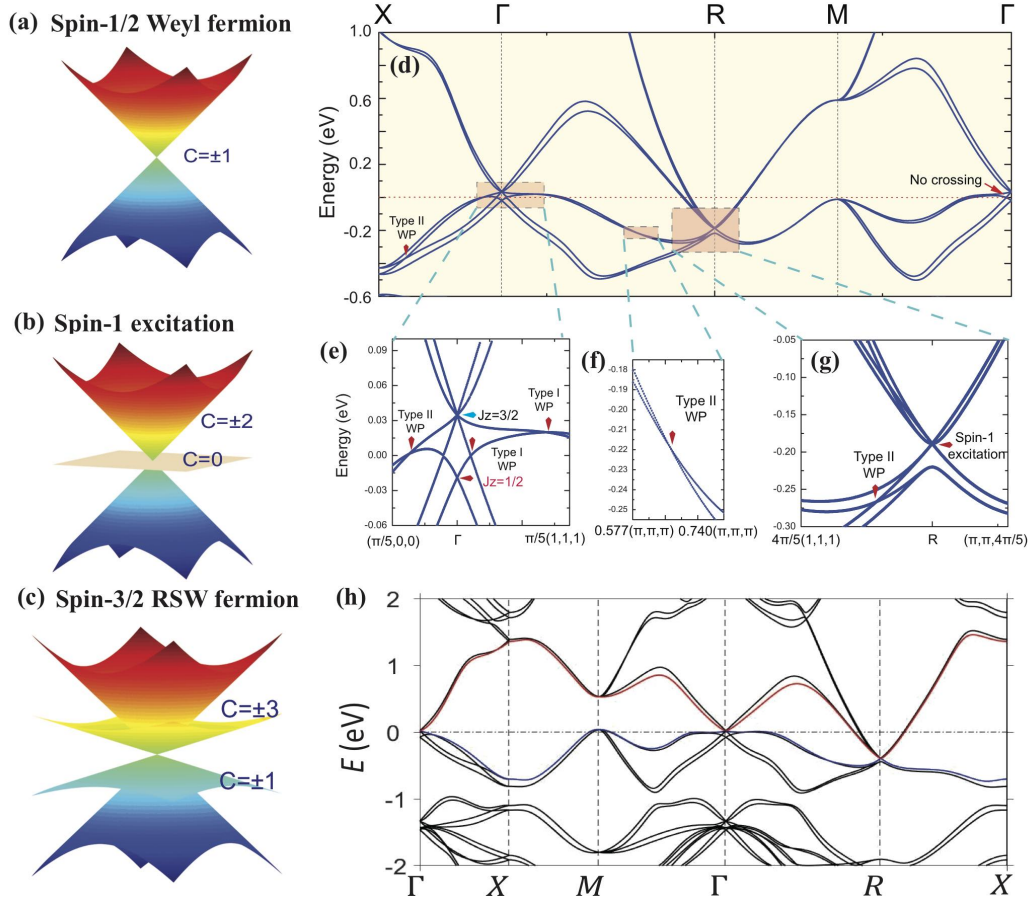


**Figure 10**

**Topological fermions with higher spin.** Panels (a)–(c) show the low-energy dispersions of  $j = 1/2$ ,  $j = 1$ , and  $j = 3/2$  fermions, respectively, based on Eq. (8). The Chern numbers associated with these bands are indicated. Also shown are the bulk band structures of cubic silicides CoSi and RhSi in space group 198 ( $P2_13$ ) in the presence of spin-orbit coupling. Panel (a) shows the band structure of CoSi along high symmetry lines, which exhibits a fourfold-degenerate spin  $j = 3/2$  fermion at  $\Gamma$  and a sixfold degenerate fermion at  $R$ . These are shown more clearly in the enlargements of panels (b) and (d), respectively. The sixfold fermion at  $R$  can be described by a double spin  $j = 1$  fermion, as indicated in panel (d); the  $j = 3/2$  fermion at  $\Gamma$  is marked by a blue arrow in (b). (Additional twofold Weyl points are present as well.) Panel (e) shows the band structure of RhSi with qualitatively the same features. For both materials the fourfold-degenerate fermion at  $\Gamma$  lies at the Fermi energy, whereas the double spin  $j = 1$  fermion sits below the Fermi energy. Adapted from Ref. (156) and (157).

momentum measured relative to the degeneracy point and  $\sigma$  are the Pauli matrices. As such, the Weyl Hamiltonian describes a low-energy gapless fermion with spin  $j = 1/2$ . The generalization to higher spin is then straightforward and is achieved by replacing the Pauli spin matrices with the corresponding higher spin matrices. Specifically, the simplest Hamiltonian sufficient to capture the generic properties of higher spin fermions is given by

$$H(\mathbf{k}) = v_0 \delta \mathbf{k} \cdot \mathbf{S}, \quad [S_i, S_j] = i \epsilon_{ijk} S_k, \quad (8)$$

where  $\mathbf{S} = (S_x, S_y, S_z)$  are three spin matrices of a spin- $j$  fermion satisfying the canonical  $SU(2)$  algebra. At  $\delta\mathbf{k} = 0$  the bands are  $2j + 1$ -fold degenerate, which shows that  $j = 1$  and  $j = 3/2$  fermions describe threefold and fourfold band crossings, respectively. The band dispersion of  $j = 1$  and  $j = 3/2$  fermions with Hamiltonian (8) is shown in Figs. 10(b) and (c), which may be contrasted with the Weyl fermion shown in Fig. 10(a).

Higher spin fermions are topological in the sense that they describe band crossings with net Berry monopole charge. The Berry flux associated with each band can be inferred from its rotation eigenvalues and gives  $2j_z$  for  $j_z = -j, -j + 1, \dots, j$ . For the  $j = 1$  and  $j = 3/2$  fermions described by (8) this implies that they carry monopole charge  $C = \pm 2$  and  $C = \pm 3 \pm 1 = \pm 4$ , respectively (see Fig. 10). This may be compared to the Weyl fermion, which has monopole charge  $C = \pm 1$ .

Even though Weyl fermions belong to the class of chiral topological fermions described by a Hamiltonian of the form of Eq. (8), it should be noted that Weyl fermions can occur at a generic point in the Brillouin zone, whereas fermions with higher spin can only occur at high-symmetry points. As mentioned in Section 5.1, the threefold fermions with spin  $j = 1$  can only occur at high-symmetry points of the Brillouin zone boundary and require a nonsymmorphic space group. In contrast, the fourfold-degenerate band crossings with spin  $j = 3/2$  structure do not strictly rely on the nonsymmorphic nature of the space group and can occur for symmorphic space groups (13). The latter is not surprising, as it follows directly from the well-known fact that cubic double point groups can protect the degeneracy of a  $j = 3/2$  quartet.

To showcase the space group classification of higher spin fermions, Bradlyn *et al.* proposed a number of material candidates to realize such semimetallic phases and supported these proposals with first-principles band structure calculations. Examples of materials predicted to exhibit threefold band crossings relatively close to the Fermi level are  $\text{Pd}_3\text{Bi}_2\text{S}_2$  (space group 199) and  $\text{Ag}_3\text{Se}_2\text{Au}$  (space group 214). Furthermore,  $\text{Ag}_3\text{Se}_2\text{Au}$  was found to exhibit a fourfold band crossing at  $\Gamma$ , which is very close to the Fermi level.

As part of this wave of proposals, topological fermions with higher spin were also predicted in a family of cubic silicide materials  $\text{ASi}$  and  $\text{AGe}$  ( $A = \text{Rh, Co}$ ) in space group 198 ( $P2_13$ ) (157, 156). Figure 10 shows the bulk band structure of  $\text{CoSi}$  and  $\text{RhSi}$  reported in Refs. (157, 156), which exhibit a  $j = 3/2$  fermion at  $\Gamma$  sitting at the Fermi energy and a sixfold-degenerate fermion at  $R$ . The latter is described by two copies of (8) and can thus be understood as a double spin  $j = 1$  fermion. The Berry monopole charge associated with these fermions (*i.e.* the Chern numbers) exactly cancel ( $4 - 2 \times 2 = 0$ ), as required by the Nielsen-Ninomiya theorem (79) mentioned in Section 3. The semimetallic nature of  $\text{CoSi}$  and  $\text{RhSi}$  finds its origin in a combination of electron filling, space group symmetry, and  $\mathcal{T}$  symmetry, which puts these materials in the class of filling-enforced semimetals (158, 151, 74).

### 5.3. Triple-point semimetals

The multifold band crossings considered in Sections 5.1 and 5.2 occur at special high-symmetry points in the Brillouin zone and are associated with higher dimensional space group representations of the corresponding little group. This is, however, not the only way in which stable threefold degenerate band crossings can arise in band structures. A symmetry-protected crossing of three energy bands can also occur at a (generic) point on a high-symmetry line, provided the little group of the high-symmetry line admits both one- and two-dimensional (double) group representations. This is true for threefold rotation axes with little group  $C_{3v}$  and threefold band crossings of this kind have been identified as “triple-point” semimetals (14, 15, 16, 17).

The origin of triple-point semimetals can be traced back to a band inversion. As explained in the context of Dirac semimetals in Section 2.1, band inversions can give rise to stable band

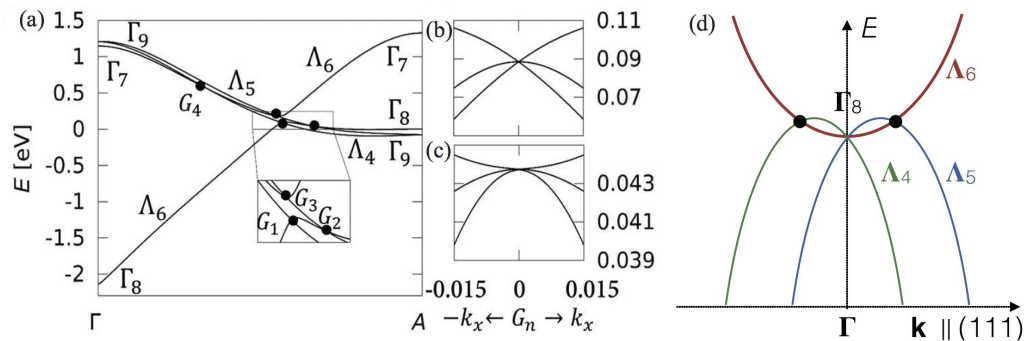


**Figure 11**

**Triple-point semimetal.** Panel (a): Band structure of ZrTe along the  $\Gamma$ -A line. Bands are labeled by their double group representations corresponding to  $D_{3h}$  at  $\Gamma$  and A points and  $C_{3v}$  on the  $\Gamma$ -A line. Panels (b) and (c) show band structures in the (100) direction with  $k_z$  tuned to the TPs  $G_1$  and  $G_2$ . Panel (d) shows the schematic band structure of unstrained HgTe near  $\Gamma$ . Adapted from Ref. (14)

crossings in the presence of symmetries, in particular rotation symmetry. To understand the origin of triple-point degeneracies one may consider the example of  $j_z = \pm 1/2$  and  $j_z = \pm 3/2$  bands inverting at  $\Gamma$ . Along the rotation axis with little group  $C_{3v}$  the  $j_z = \pm 1/2$  states must stick together, but the  $j_z = \pm 3/2$  state generically split (except at  $\mathcal{T}$ -invariant points). This provides a simple picture of triple-point degeneracies and explains why they come in pairs. In addition, this example immediately reveals that further splitting the twofold degeneracy along the rotation axis by breaking appropriate symmetries results in a Weyl semimetal.

The first proposals for observing this new type of TSM in real materials were focused on a family of two-element metals  $AB$  with tungsten carbide (WC) structure, where  $A = \{\text{Zr, Nb, Mo, Ta, W}\}$  and  $B = \{\text{C, N, P, S, Te}\}$  (14, 15, 16). The band structure of ZrTe is shown in Fig. 11. Strained HgTe along the (111) direction was suggested as another venue for these triple point band crossings (14). Since HgTe is structurally related to the half-Heusler compounds (the latter crystallize in a stuffed zincblende structure) and have similar electronic structure (159), subsequent work expanded the search for triple-point semimetals to this material class (160). The layered trigonal material PtBi<sub>2</sub> was proposed as yet another possible venue (161). Remarkably, angle-resolved photoemission measurements performed on MoP (34) and WC (35) have since led to a first report of experimental observation of triple-point fermions.

## 6. STRATEGIES FOR MATERIAL PREDICTION AND DESIGN

In this final section we discuss recent developments in the design and implementation of systematic materials search strategies, geared towards the prediction novel TSMs. The proposals for material realizations discussed in this review originated from the attempt to find examples of a specific type of TSM. In these targeted searches, identification of materials or material classes was predicated on the specific symmetry requirements and electrochemical parameters (*e.g.* orbital composition, spin-orbit coupling) associated with a particular TSM, and in many cases a great deal of physical or chemical intuition was involved. As successful as such approaches based on expertise and experience have proven to be, the goal to perform more systematic and algorithmic searches of known synthesized materials has motivated attempts to put the classification and diagnosis of topological electronic band structures on a new footing.

These attempts have led to a set of recent ideas centered around the notion of symmetry indicators (162, 163, 164, 165, 140). The general philosophy underlying these ideas is to use the symmetry quantum numbers characterizing a band structure (*e.g.* space group representations at high-symmetry points), as well as the constraints which these must satisfy (*e.g.* compatibility relations), and infer from this symmetry data the topological characteristics of the band structure, *i.e.* the topological data. Specific cases where such an approach applies were known, as for instance the inversion-eigenvalue formula for detecting Weyl points (166), and the methods relying on symmetry indicators promote these specific examples to a comprehensive and systematic framework. This is particularly powerful in the context of first-principles calculations, in which the symmetry data is more readily accessible than the topological data.

Remarkably, a series of very recent works have employed this set of ideas to systematically search large material databases for previously unrecognized topological materials, both insulators and semimetals (167, 168, 169). Based on high-throughput computational schemes, thousands of new topological materials were identified, constituting an encouraging step forward in the quest for new and better topological materials.

## 7. SUMMARY AND OUTLOOK

In this review we have given an overview of some recent developments in the field of TSMs. In addition to the Dirac and Weyl semimetal phases, which provide condensed matter realizations of Dirac and Weyl fermions, our survey has focused on some more recent examples of TSMs, such as nodal line semimetals, multifold fermion semimetals, and triple-point fermion semimetals. In a broad sense, two concepts were shown to be central to the understanding of TSMs: the notion of symmetry-enforced band crossings and the notion of a band inversion. The latter establishes a direct connection to other classes of topological materials, such as topological insulators and topological crystalline insulators. The examples of proposed material realizations discussed in this review showcase the importance of first-principles band structure calculations for the prediction of new topological materials, in particular TSMs.

A number of important and exciting challenges lie ahead. Building on the encouraging experimental observation of some of these TSMs, future efforts will concentrate on identifying “ideal” versions of TSMs in real materials. TSMs can be called ideal when the low-energy gapless fermions sit at the Fermi energy and do not overlap in energy with other (non-topological) band structure features. Another direction for the future is to explore the properties of TSMs in more detail, such as transport and optical properties. The ability to control and manipulate these properties will be a prerequisite for using TSMs as a resource for quantum devices.

## DISCLOSURE STATEMENT

If the authors have nothing to disclose, the following statement will be used: The authors are not aware of any affiliations, memberships, funding, or financial holdings that might be perceived as affecting the objectivity of this review.

## ACKNOWLEDGMENTS

Our own research in the general area of topological materials has greatly benefited from current and past collaborations with many distinguished colleagues. We feel particularly indebted to Liang Fu, Charles Kane, Eugene Mele, Benjamin Wieder, Steven Young, Saad Zaheer. We owe special thanks to Benjamin Wieder and Eugene Mele for helpful correspondence and a careful reading of a

draft version of the manuscript. JWFV was supported by the National Science Foundation MRSEC Program, under grant DMR-1720530. YK was supported from Institute for Basic Science (IBS-R011-D1) and a National Research Foundation of Korea (NRF) grant (NRF-2017R1C1B5018169). AMR was supported by the Department of Energy, Office of Basic Energy Sciences, under grant DE-FG02-07ER46431.

## LITERATURE CITED

1. Hasan MZ, Kane CL. 2010. *Colloquium* : Topological insulators. *Rev. Mod. Phys.* 82:3045–3067
2. Qi XL, Zhang SC. 2011. Topological insulators and superconductors. *Rev. Mod. Phys.* 83:1057–1110
3. Armitage NP, Mele EJ, Vishwanath A. 2018. Weyl and dirac semimetals in three-dimensional solids. *Rev. Mod. Phys.* 90:015001
4. Young SM, Zaheer S, Teo JCY, Kane CL, Mele EJ, Rappe AM. 2012. Dirac semimetal in three dimensions. *Phys. Rev. Lett.* 108:140405
5. Wang Z, Sun Y, Chen XQ, Franchini C, Xu G, et al. 2012. Dirac semimetal and topological phase transitions in  $A_3Bi$  ( $a = Na, k, rb$ ). *Phys. Rev. B* 85:195320
6. Wan X, Turner AM, Vishwanath A, Savrasov SY. 2011. Topological semimetal and fermi-arc surface states in the electronic structure of pyrochlore iridates. *Phys. Rev. B* 83:205101
7. Weng H, Fang C, Fang Z, Bernevig BA, Dai X. 2015. Weyl semimetal phase in noncentrosymmetric transition-metal monophosphides. *Phys. Rev. X* 5:011029
8. Hořava P. 2005. Stability of fermi surfaces and  $k$  theory. *Phys. Rev. Lett.* 95:016405
9. Heikkilä TT, Volovik GE. 2011. Dimensional crossover in topological matter: Evolution of the multiple dirac point in the layered system to the flat band on the surface. *JETP Lett.* 93:59–65
10. Burkov A, Hook M, Balents L. 2011. Topological nodal semimetals. *Phys. Rev. B* 84:235126
11. Soluyanov AA, Gresch D, Wang Z, Wu Q, Troyer M, et al. 2015. Type-ii weyl semimetals. *Nature* 527:495–498
12. Wieder BJ, Kim Y, Rappe AM, Kane CL. 2016. Double dirac semimetals in three dimensions. *Phys. Rev. Lett.* 116:186402
13. Bradlyn B, Cano J, Wang Z, Vergniory M, Felser C, et al. 2016. Beyond dirac and weyl fermions: Unconventional quasiparticles in conventional crystals. *Science* 353:5037
14. Zhu Z, Winkler GW, Wu Q, Li J, Soluyanov AA. 2016. Triple point topological metals. *Phys. Rev. X* 6:031003
15. Weng H, Fang C, Fang Z, Dai X. 2016. Topological semimetals with triply degenerate nodal points in  $\theta$ -phase tantalum nitride. *Phys. Rev. B* 93:241202
16. Chang G, Xu SY, Huang SM, Sanchez DS, Hsu CH, et al. 2017. Nexus fermions in topological symmetric crystalline metals. *Sci. Rep.* 7:1688
17. Wieder BJ. 2018. Threes company. *Nat. Phys.* 14:329
18. Jeon S, Zhou BB, Gyenis A, Feldman BE, Kimchi I, et al. 2014. Landau quantization and quasiparticle interference in the three-dimensional dirac semimetal  $cd_3$  as  $2$ . *Nat. Mater.* 13:851
19. Feng J, Pang Y, Wu D, Wang Z, Weng H, et al. 2015. Large linear magnetoresistance in dirac semimetal  $cd_3$  as  $2$  with fermi surfaces close to the dirac points. *Phys. Rev. B* 92:081306
20. Zhang C, Xu SY, Belopolski I, Yuan Z, Lin Z, et al. 2015. Observation of the adler-bell-jackiw chiral anomaly in a weyl semimetal. *arXiv preprint arXiv:1503.02630*
21. Huang X, Zhao L, Long Y, Wang P, Chen D, et al. 2015. Observation of the chiral-anomaly-induced negative magnetoresistance in 3d weyl semimetal  $taas$ . *Phys. Rev. X* 5:031023
22. Wang Y, Liu E, Liu H, Pan Y, Zhang L, et al. 2016. Gate-tunable negative longitudinal magnetoresistance in the predicted type-ii weyl semimetal  $wte_2$ . *Nat. Commun.* 7:13142
23. Rajamathi CR, Gupta U, Kumar N, Yang H, Sun Y, et al. 2017. Weyl semimetals as hydrogen evolution catalysts. *Adv. Mater.* 29:1606202
24. Li J, Ma H, Xie Q, Feng S, Ullah S, et al. 2018. Topological quantum catalyst: Dirac nodal line states and a potential electrocatalyst of hydrogen evolution in the tisi family. *Sci. China Mater.* 61:23–29
25. Nayak C, Simon SH, Stern A, Freedman M, Das Sarma S. 2008. Non-abelian anyons and topological

- quantum computation. *Rev. Mod. Phys.* 80:1083–1159
26. Yang SA. 2016. Dirac and weyl materials: fundamental aspects and some spintronics applications. In *Spin*, vol. 6. World Scientific
  27. Herring C. 1937. Accidental degeneracy in the energy bands of crystals. *Phys. Rev.* 52:365
  28. Yang BJ, Morimoto T, Furusaki A. 2015. Topological charges of three-dimensional dirac semimetals with rotation symmetry. *Phys. Rev. B* 92:165120
  29. Yu R, Qi XL, Bernevig A, Fang Z, Dai X. 2011. Equivalent expression of  $F_2$  topological invariant for band insulators using the non-abelian berry connection. *Phys. Rev. B* 84:075119
  30. Bansil A, Lin H, Das T. 2016. Colloquium: Topological band theory. *Rev. Mod. Phys.* 88:021004
  31. Yu R, Fang Z, Dai X, Weng H. 2017. Topological nodal line semimetals predicted from first-principles calculations. *Front. Phys.* 12:127202
  32. Hirayama M, Okugawa R, Murakami S. 2018. Topological semimetals studied by ab initio calculations. *J. Phys. Soc. Jpn.* 87:041002
  33. Huang SM, Xu SY, Belopolski I, Lee CC, Chang G, et al. 2015. A weyl fermion semimetal with surface fermi arcs in the transition metal monopnictide taas class. *Nat. Commun.* 6:7373
  34. Lv B, Feng ZL, Xu QN, Gao X, Ma JZ, et al. 2017. Observation of three-component fermions in the topological semimetal molybdenum phosphide. *Nature* 546:627
  35. Ma JZ, He JB, Xu YF, Lv B, Chen D, et al. 2018. Three-component fermions with surface fermi arcs in tungsten carbide. *Nat. Phys.* 14:349
  36. Neupane M, Belopolski I, Hosen MM, Sanchez DS, Sankar R, et al. 2016. Observation of topological nodal fermion semimetal phase in zrsis. *Phys. Rev. B* 93:201104
  37. Turner AM, Vishwanath A, Head CO. 2013. Beyond band insulators: topology of semimetals and interacting phases. *Topological Insulators* 6:293–324
  38. Wehling T, Black-Schaffer AM, Balatsky AV. 2014. Dirac materials. *Adv. Phys.* 63:1–76
  39. Vafeek O, Vishwanath A. 2014. Dirac fermions in solids: From high- $t_c$  cuprates and grapheneo opological insulators and weyl semimetals. *Annu. Rev. Condens. Matter Phys.* 5:83–112
  40. Hasan MZ, Xu SY, Bian G. 2015. Topological insulators, topological superconductors and weyl fermion semimetals: discoveries, perspectives and outlooks. *Phys. Scr.* 2015:014001
  41. Weng H, Dai X, Fang Z. 2016. Topological semimetals predicted from first-principles calculations. *J. Phys. Condens. Matter* 28:303001
  42. Fang C, Weng H, Dai X, Fang Z. 2016. Topological nodal line semimetals. *Chin. Phys. B* 25:117106
  43. Jia S, Xu SY, Hasan MZ. 2016. Weyl semimetals, fermi arcs and chiral anomalies. *Nat. Mater.* 15:1140
  44. Yan B, Felser C. 2017. Topological materials: Weyl semimetals. *Annu. Rev. Condens. Matter Phys.* 8:337–354
  45. Hasan MZ, Xu SY, Belopolski I, Huang SM. 2017. Discovery of weyl fermion semimetals and topological fermi arc states. *Annu. Rev. Condens. Matter Phys.* 8:289–309
  46. Yang SY, Yang H, Derunova E, Parkin SS, Yan B, Ali MN. 2018. Symmetry demanded topological nodal-line materials. *Advances in Physics: X* 3:1414631
  47. Burkov A. 2018. Weyl metals. *Annu. Rev. Condens. Matter Phys.* 9:359–378
  48. Schoop LM, Pielhofer F, Lotsch BV. 2018. Chemical principles of topological semimetals. *Chem. Mater.* 30:3155–3176
  49. Bernevig A, Weng H, Fang Z, Dai X. 2018. Recent progress in the study of topological semimetals. *J. Phys. Soc. Jpn.* 87:041001
  50. Murakami S. 2007. Phase transition between the quantum spin hall and insulator phases in 3d: emergence of a topological gapless phase. *New J. Phys.* 9:356
  51. Neto AC, Guinea F, Peres NM, Novoselov KS, Geim AK. 2009. The electronic properties of graphene. *Rev. Mod. Phys.* 81:109
  52. Novoselov KS, Geim AK, Morozov SV, Jiang D, Zhang Y, et al. 2004. Electric field effect in atomically thin carbon films. *Science* 306:666–669
  53. Weng H, Dai X, Fang Z. 2014. Transition-metal pentatelluride zrte 5 and hfte 5: A paradigm for large-gap quantum spin hall insulators. *Phys. Rev. X* 4:011002
  54. Gibson QD, Schoop LM, Muechler L, Xie LS, Hirschberger M, et al. 2015. Three-dimensional dirac



- semimetals: Design principles and predictions of new materials. *Phys. Rev. B* 91:205128
55. Manzoni G, Gragnaniello L, Autès G, Kuhn T, Sterzi A, et al. 2016. Evidence for a strong topological insulator phase in  $\text{zrte}_5$ . *Phys. Rev. Lett.* 117:237601
  56. Li Q, Kharzeev DE, Zhang C, Huang Y, Pletikosić I, et al. 2016. Chiral magnetic effect in  $\text{zrte}_5$ . *Nat. Phys.* 12:550
  57. Zhang Y, Wang C, Yu L, Liu G, Liang A, et al. 2017. Electronic evidence of temperature-induced lifshitz transition and topological nature in  $\text{zrte}_5$ . *Nat. Commun.* 8:15512
  58. Mutch J, Chen WC, Went P, Qian T, Wilson IZ, et al. 2018. Evidence for a strain tuned topological phase transition in  $\text{zrte}_5$ . *arXiv preprint arXiv:1808.07898*
  59. Kane CL, Mele EJ. 2005. Quantum spin hall effect in graphene. *Phys. Rev. Lett.* 95:226801
  60. Young SM, Kane CL. 2015. Dirac semimetals in two dimensions. *Phys. Rev. Lett.* 115:126803
  61. Zaheer S. 2014. Three dimensional dirac semimetals. Ph.D. thesis, University of Pennsylvania
  62. Steinberg JA, Young SM, Zaheer S, Kane CL, Mele EJ, Rappe AM. 2014. Bulk dirac points in distorted spinels. *Phys. Rev. Lett.* 112:036403
  63. Wang Z, Weng H, Wu Q, Dai X, Fang Z. 2013. Three-dimensional dirac semimetal and quantum transport in  $\text{cd}_3\text{as}_2$ . *Phys. Rev. B* 88:125427
  64. Du Y, Wan B, Wang D, Sheng L, Duan CG, Wan X. 2015. Dirac and weyl semimetal in  $\text{xybi}$  ( $x = \text{ba}$ ,  $\text{eu}$ ;  $y = \text{cu}$ ,  $\text{ag}$  and  $\text{au}$ ). *Sci. Rep.* 5:14423
  65. Cao W, Tang P, Xu Y, Wu J, Gu BL, Duan W. 2017. Dirac semimetal phase in hexagonal  $\text{liznbi}$ . *Phys. Rev. B* 96:115203
  66. Yang BJ, Nagaosa N. 2014. Classification of stable three-dimensional dirac semimetals with nontrivial topology. *Nat. Commun.* 5:4898
  67. Liu Z, Zhou B, Zhang Y, Wang Z, Weng H, et al. 2014. Discovery of a three-dimensional topological dirac semimetal,  $\text{na}_3\text{bi}$ . *Science* 343:864–867
  68. Liu Z, Jiang J, Zhou B, Wang Z, Zhang Y, et al. 2014. A stable three-dimensional topological dirac semimetal  $\text{cd}_3\text{as}_2$ . *Nat. Mater.* 13:677–681
  69. Gao Z, Hua M, Zhang H, Zhang X. 2016. Classification of stable dirac and weyl semimetals with reflection and rotational symmetry. *Phys. Rev. B* 93:205109
  70. Chen C, Wang SS, Liu L, Yu ZM, Sheng XL, et al. 2017. Ternary wurtzite  $\text{caagbi}$  materials family: A playground for essential and accidental, type-i and type-ii dirac fermions. *Phys. Rev. Materials* 1:044201
  71. Gao H, Kim Y, Venderbos JWF, Kane CL, Mele EJ, et al. 2018. Dirac-weyl semimetal: Coexistence of dirac and weyl fermions in polar hexagonal  $\text{abc}$  crystals. *Phys. Rev. Lett.* 121:106404
  72. Liu Q, Zunger A. 2017. Predicted realization of cubic dirac fermion in quasi-one-dimensional transition-metal monochalcogenides. *Phys. Rev. X* 7:021019
  73. Tang P, Zhou Q, Xu G, Zhang SC. 2016. Dirac fermions in an antiferromagnetic semimetal. *Nat. Phys.* 12:1100
  74. Young SM, Wieder BJ. 2017. Filling-enforced magnetic dirac semimetals in two dimensions. *Phys. Rev. Lett.* 118:186401
  75. Wang J. 2017. Magnetic dirac semimetals in three dimensions. *arXiv preprint arXiv:1701.00896*
  76. Watanabe H, Po HC, Vishwanath A. 2018. Structure and topology of band structures in the 1651 magnetic space groups. *Sci. Adv.* 4:eaat8685
  77. Hua G, Nie S, Song Z, Yu R, Xu G, Yao K. 2018. Dirac semimetal in type iv magnetic space group. *arXiv preprint arXiv:1801.02806*
  78. Schoop LM, Topp A, Lippmann J, Orlandi F, Mùchler L, et al. 2018. Tunable weyl and dirac states in the nonsymmorphic compound  $\text{cesbte}$ . *Sci. Adv.* 4:eaar2317
  79. Nielsen HB, Ninomiya M. 1983. The adler-bell-jackiw anomaly and weyl fermions in a crystal. *Physics Letters B* 130:389–396
  80. Xu G, Weng H, Wang Z, Dai X, Fang Z. 2011. Chern semimetal and the quantized anomalous hall effect in  $\text{hgcr}_2\text{se}_4$ . *Phys. Rev. Lett.* 107:186806
  81. Wang Z, Vergniory M, Kushwaha S, Hirschberger M, Chulkov E, et al. 2016. Time-reversal-breaking weyl fermions in magnetic heusler alloys. *Phys. Rev. Lett.* 117:236401

82. Chang G, Xu SY, Zheng H, Singh B, Hsu CH, et al. 2016. Room-temperature magnetic topological weyl fermion and nodal line semimetal states in half-metallic heusler  $\text{Co}_2\text{TiX}$  ( $X = \text{Si, Ge, or Sn}$ ). *Sci. Rep.* 6:38839
83. Yang H, Sun Y, Zhang Y, Shi WJ, Parkin SS, Yan B. 2017. Topological weyl semimetals in the chiral antiferromagnetic materials  $\text{Mn}_3\text{Ge}$  and  $\text{Mn}_3\text{Sn}$ . *New J. Phys.* 19:015008
84. Xu Q, Liu E, Shi W, Muechler L, Gayles J, et al. 2018. Topological surface fermi arcs in the magnetic weyl semimetal  $\text{Co}_3\text{Sn}_2\text{S}_2$ . *Phys. Rev. B* 97:235416
85. Nayak AK, Fischer JE, Sun Y, Yan B, Karel J, et al. 2016. Large anomalous hall effect driven by a nonvanishing berry curvature in the noncolinear antiferromagnet  $\text{Mn}_3\text{Ge}$ . *Sci. Adv.* 2:e1501870
86. Kiyohara N, Tomita T, Nakatsuji S. 2016. Giant anomalous hall effect in the chiral antiferromagnet  $\text{Mn}_3\text{Ge}$ . *Phys. Rev. Appl.* 5:064009
87. Liu E, Sun Y, Kumar N, Muechler L, Sun A, et al. 2018. Giant anomalous hall effect in a ferromagnetic kagome-lattice semimetal. *Nat. Phys.* :1
88. Wang Q, Xu Y, Lou R, Liu Z, Li M, et al. 2018. Large intrinsic anomalous hall effect in half-metallic ferromagnet  $\text{Co}_3\text{Sn}_2\text{S}_2$  with magnetic weyl fermions. *Nat. Commun.* 9:3681
89. Burkov A, Balents L. 2011. Weyl semimetal in a topological insulator multilayer. *Phys. Rev. Lett.* 107:127205
90. Zhang H, Wang J, Xu G, Xu Y, Zhang SC. 2014. Topological states in ferromagnetic  $\text{CdO}/\text{EuO}$  superlattices and quantum wells. *Phys. Rev. Lett.* 112:096804
91. Liu J, Vanderbilt D. 2014. Weyl semimetals from noncentrosymmetric topological insulators. *Phys. Rev. B* 90:155316
92. Zyuzin AA, Wu S, Burkov AA. 2012. Weyl semimetal with broken time reversal and inversion symmetries. *Phys. Rev. B* 85:165110
93. Halász GB, Balents L. 2012. Time-reversal invariant realization of the weyl semimetal phase. *Phys. Rev. B* 85:035103
94. Xu SY, Alidoust N, Belopolski I, Yuan Z, Bian G, et al. 2015. Discovery of a weyl fermion state with fermi arcs in niobium arsenide. *Nat. Phys.* 11:748
95. Xu SY, Belopolski I, Alidoust N, Neupane M, Bian G, et al. 2015. Discovery of a weyl fermion semimetal and topological fermi arcs. *Science* 349:613–617
96. Lv B, Weng H, Fu B, Wang X, Miao H, et al. 2015. Experimental discovery of weyl semimetal  $\text{TaAs}$ . *Phys. Rev. X* 5:031013
97. Lv B, Xu N, Weng H, Ma J, Richard P, et al. 2015. Observation of weyl nodes in  $\text{TaAs}$ . *Nature Physics* 11:724
98. Yang L, Liu Z, Sun Y, Peng H, Yang H, et al. 2015. Weyl semimetal phase in the non-centrosymmetric compound  $\text{TaAs}$ . *Nat. Phys.* 11:728
99. Bernevig BA. 2015. It's been a weyl coming. *Nat. Phys.* 11:698
100. Ruan J, Jian SK, Zhang D, Yao H, Zhang H, et al. 2016. Ideal weyl semimetals in the chalcopyrites  $\text{CuTe}_2$ ,  $\text{AgTe}_2$ ,  $\text{AuTe}_2$ , and  $\text{ZnPtAs}_2$ . *Phys. Rev. Lett.* 116:226801
101. Autes G, Gresch D, Troyer M, Soluyanov AA, Yazyev OV. 2016. Robust type-ii weyl semimetal phase in transition metal diphosphides  $\text{X}_2\text{P}_2$  ( $X = \text{Mo, W}$ ). *Phys. Rev. Lett.* 117:066402
102. Chang G, Xu SY, Sanchez DS, Huang SM, Lee CC, et al. 2016. A strongly robust type ii weyl fermion semimetal state in  $\text{Ta}_3\text{S}_2$ . *Sci. Adv.* 2:e1600295
103. Koepf K, Kasinathan D, Efremov D, Khim S, Borisenko S, et al. 2016.  $\text{TaIrTe}_4$ : a ternary type-ii weyl semimetal. *Phys. Rev. B* 93:201101
104. Wang Z, Gresch D, Soluyanov AA, Xie W, Kushwaha S, et al. 2016.  $\text{MnTe}_2$ : a type-ii weyl topological metal. *Phys. Rev. Lett.* 117:056805
105. Chang G, Sanchez DS, Wieder BJ, Xu SY, Schindler F, et al. 2016. Universal topological electronic properties of nonmagnetic chiral crystals. *arXiv preprint arXiv:1611.07925*
106. Morimoto T, Zhong S, Orenstein J, Moore JE. 2016. Semiclassical theory of nonlinear magneto-optical responses with applications to topological Dirac/Weyl semimetals. *Physical Review B* 94:245121
107. de Juan F, Grushin AG, Morimoto T, Moore JE. 2017. Quantized circular photogalvanic effect in Weyl semimetals. *Nature Communications* 8:15995

108. Wu L, Patankar S, Morimoto T, Nair NL, Thewalt E, et al. 2017. Giant anisotropic nonlinear optical response in transition metal monpnictide weyl semimetals. *Nature Physics* 13:350
109. Ma Q, Xu SY, Chan CK, Zhang CL, Chang G, et al. 2017. Direct optical detection of Weyl fermion chirality in a topological semimetal. *Nature Physics* 13:842–847
110. Yang X, Burch K, Ran Y. 2017. Divergent bulk photovoltaic effect in Weyl semimetals. *arXiv preprint arXiv:1712.09363*
111. Flicker F, de Juan F, Bradlyn B, Morimoto T, Vergniory MG, Grushin AG. 2018. Chiral Optical Response of Multifold Fermions. *arXiv preprint arXiv:1806.09642*
112. Huang H, Zhou S, Duan W. 2016. Type-II Dirac fermions in the  $pt_2$  class of transition metal dichalcogenides. *Phys. Rev. B* 94:121117
113. Xu SY, Alidoust N, Chang G, Lu H, Singh B, et al. 2016. Discovery of Lorentz-violating Weyl fermion semimetal state in layered materials. *arXiv preprint arXiv:1603.07318*
114. Chang TR, Xu SY, Sanchez DS, Tsai WF, Huang SM, et al. 2017. Type-II symmetry-protected topological Dirac semimetals. *Phys. Rev. Lett.* 119:026404
115. Fang C, Gilbert MJ, Dai X, Bernevig BA. 2012. Multi-Weyl topological semimetals stabilized by point group symmetry. *Phys. Rev. Lett.* 108:266802
116. Huang SM, Xu SY, Belopolski I, Lee CC, Chang G, et al. 2016. New type of Weyl semimetal with quadratic double Weyl fermions. *Proc. Natl. Acad. Sci. U.S.A* 113:1180–1185
117. Fang C, Chen Y, Kee HY, Fu L. 2015. Topological nodal line semimetals with and without spin-orbital coupling. *Phys. Rev. B* 92:081201
118. He J, Kong X, Wang W, Kou SP. 2018. Type-II nodal line semimetal. *New J. Phys.* 20:053019
119. Kim D, Ahn S, Jung JH, Min H, Ihm J, et al. 2018. Type-II Dirac line node in strained  $Na_3N$
120. Bzdušek T, Wu Q, Rüegg A, Sigrist M, Soluyanov AA. 2016. Nodal-chain metals. *Nature* 538:75–78
121. Kim Y, Wieder BJ, Kane CL, Rappe AM. 2015. Dirac line nodes in inversion-symmetric crystals. *Phys. Rev. Lett.* 115:036806
122. Fu L, Kane CL, Mele EJ. 2007. Topological insulators in three dimensions. *Phys. Rev. Lett.* 98:106803
123. Fu L, Kane CL. 2007. Topological insulators with inversion symmetry. *Phys. Rev. B* 76:045302
124. Teo JCY, Kane CL. 2010. Topological defects and gapless modes in insulators and superconductors. *Phys. Rev. B* 82:115120
125. Zhao J, Yu R, Weng H, Fang Z. 2016. Topological node-line semimetal in compressed black phosphorus. *Phys. Rev. B* 94:195104
126. Xu N, Qian YT, Wu QS, Autès G, Matt CE, et al. 2018. Trivial topological phase of  $CaAgP$  and the topological nodal-line transition in  $CaAg(p1-xAsx)$ . *Phys. Rev. B* 97
127. Volovik GE. 2015. From standard model of particle physics to room-temperature superconductivity. *Phys. Scr.* T164:014014
128. Heikkilä TT, Volovik GE. 2016. Flat bands as a route to high-temperature superconductivity in graphite. In *Basic Physics of Functionalized Graphite*. Springer International Publishing, 123–143
129. Yu R, Weng H, Fang Z, Dai X, Hu X. 2015. Topological node-line semimetal and Dirac semimetal state in antiperovskite  $Cu_3PdN$ . *Phys. Rev. Lett.* 115:036807
130. Mikitik GP, Sharlai YV. 1999. Manifestation of Berry's phase in metal physics. *Phys. Rev. Lett.* 82:2147–2150
131. Mikitik GP, Sharlai YV. 2006. Band-contact lines in the electron energy spectrum of graphite. *Phys. Rev. B* 73:235112
132. Schoop LM, Ali MN, Straßer C, Topp A, Varykhalov A, et al. 2016. Dirac cone protected by nonsymmorphic symmetry and three-dimensional Dirac line node in  $ZrSiS$ . *Nat. Commun.* 7:11696
133. Hu J, Tang Z, Liu J, Liu X, Zhu Y, et al. 2016. Evidence of topological nodal-line fermions in  $ZrSiSe$  and  $ZrSiTe$ . *Phys. Rev. Lett.* 117
134. Hosen MM, Dimitri K, Aperis A, Maldonado P, Belopolski I, et al. 2018. Observation of gapless Dirac surface states in  $ZrGeTe$ . *Phys. Rev. B* 97
135. Hosen MM, Dhakal G, Dimitri K, Maldonado P, Aperis A, et al. 2018. Discovery of topological nodal-line fermionic phase in a magnetic material  $GdSbTe$ . *Sci. Rep.* 8
136. Zhang X, Yu ZM, Sheng XL, Yang HY, Yang SA. 2017. Coexistence of four-band nodal rings and triply

- degenerate nodal points in centrosymmetric metal diborides. *Phys. Rev. B* 95:235116
137. Yi CJ, Lv BQ, Wu QS, Fu BB, Gao X, et al. 2018. Observation of a nodal chain with dirac surface states in TiB<sub>2</sub>. *Phys. Rev. B* 97
  138. Chang TR, Pletikoscic I, Kong T, Bian G, Huang A, et al. 2017. Realization of a type-II nodal-line semimetal in Mg<sub>3</sub>Bi<sub>2</sub>
  139. Li K, Li C, Hu J, Li Y, Fang C. 2017. Dirac and nodal line magnons in three-dimensional antiferromagnets. *Phys. Rev. Lett.* 119:247202
  140. Song Z, Zhang T, Fang C. 2018. Diagnosis for nonmagnetic topological semimetals in the absence of spin-orbital coupling. *Phys. Rev. X* 8:031069
  141. Morimoto T, Furusaki A. 2014. Weyl and dirac semimetals with  $F_2$  topological charge. *Phys. Rev. B* 89:235127
  142. Zhao YX, Lu Y. 2017.  $pt$ -symmetric real dirac fermions and semimetals. *Phys. Rev. Lett.* 118:056401
  143. Ahn J, Kim D, Kim Y, Yang BJ. 2018. Band topology and linking structure of nodal line semimetals with  $Z_2$  monopole charges. *Phys. Rev. Lett.* 121:106403
  144. Nomura T, Habe T, Sakamoto R, Koshino M. 2018. Three-dimensional graphdiyne as a topological nodal-line semimetal. *Phys. Rev. Mater.* 2:054204
  145. Yamakage A, Yamakawa Y, Tanaka Y, Okamoto Y. 2016. Line-node dirac semimetal and topological insulating phase in noncentrosymmetric pnictides CaAgX (x = p, as). *J. Phys. Soc. Jpn.* 85:013708
  146. Nayak J, Kumar N, Wu SC, Shekhar C, Fink J, et al. 2018. Electronic properties of topological insulator candidate CaAgAs. *J. Phys.: Condens. Matter* 30:045501
  147. Takane D, Nakayama K, Souma S, Wada T, Okamoto Y, et al. 2018. Observation of dirac-like energy band and ring-torus fermi surface associated with the nodal line in topological insulator CaAgAs. *npj Quant. Mater.* 3
  148. Sun JP. 2017. Topological nodal line semimetal in non-centrosymmetric PbTaS<sub>2</sub>. *Chin. Phys. Lett.* 34:077101
  149. Okamoto Y, Inohara T, Yamakage A, Yamakawa Y, Takenaka K. 2016. Low carrier density metal realized in candidate line-node dirac semimetals CaAgP and CaAgAs. *J. Phys. Soc. Jpn.* 85:123701
  150. Xu CQ, Sankar R, Zhou W, Li B, Han ZD, et al. 2017. Topological phase transition under pressure in the topological nodal-line superconductor PbTaSe<sub>2</sub>. *Phys. Rev. B* 96
  151. Wieder BJ, Kane CL. 2016. Spin-orbit semimetals in the layer groups. *Phys. Rev. B* 94:155108
  152. Chen Y, Lu YM, Kee HY. 2015. Topological crystalline metal in orthorhombic perovskite iridates. *Nat. Commun.* 6
  153. Manes JL. 2012. Existence of bulk chiral fermions and crystal symmetry. *Physical Review B* 85:155118
  154. Bradlyn B, Cano J, Wang Z, Vergniory M, Felser C, et al. 2016. Beyond dirac and weyl fermions: Unconventional quasiparticles in conventional crystals. *Science* 353:aaf5037
  155. Sharma G, Zhao Z, Sarker P, Nail BA, Wang J, et al. 2016. Electronic structure, photovoltage, and photocatalytic hydrogen evolution with p-cu<sub>2</sub>o<sub>4</sub> nanocrystals. *J. Mater. Chem. A* 4:2936–2942
  156. Tang P, Zhou Q, Zhang SC. 2017. Multiple types of topological fermions in transition metal silicides. *Phys. Rev. Lett.* 119:206402
  157. Chang G, Xu SY, Wieder BJ, Sanchez DS, Huang SM, et al. 2017. Unconventional chiral fermions and large topological fermi arcs in rhsi. *Phys. Rev. Lett.* 119:206401
  158. Watanabe H, Po HC, Vishwanath A, Zaletel M. 2015. Filling constraints for spin-orbit coupled insulators in symmorphic and nonsymmorphic crystals. *Proceedings of the National Academy of Sciences* 112:14551–14556
  159. Chadov S, Qi X, Kübler J, Fecher GH, Felser C, Zhang SC. 2010. Tunable multifunctional topological insulators in ternary heusler compounds. *Nat. Mater.* 9:541
  160. Yang H, Yu J, Parkin SSP, Felser C, Liu CX, Yan B. 2017. Prediction of triple point fermions in simple half-heusler topological insulators. *Phys. Rev. Lett.* 119:136401
  161. Gao W, Zhu X, Zheng F, Wu M, Zhang J, et al. 2018. A possible candidate for triply degenerate point fermions in trigonal layered ptbi<sub>2</sub>. *Nat. Commun.* 9:3249
  162. Bradlyn B, Elcoro L, Cano J, Vergniory M, Wang Z, et al. 2017. Topological quantum chemistry. *Nature* 547:298

163. Po HC, Vishwanath A, Watanabe H. 2017. Symmetry-based indicators of band topology in the 230 space groups. *Nat. Commun.* 8:50
164. Kruthoff J, de Boer J, van Wezel J, Kane CL, Slager RJ. 2017. Topological classification of crystalline insulators through band structure combinatorics. *Phys. Rev. X* 7:041069
165. Song Z, Zhang T, Fang Z, Fang C. 2018. Quantitative mappings between symmetry and topology in solids. *Nat. Commun.* 9:3530
166. Hughes TL, Prodan E, Bernevig BA. 2011. Inversion-symmetric topological insulators. *Phys. Rev. B* 83:245132
167. Zhang T, Jiang Y, Song Z, Huang H, He Y, et al. 2018. Catalogue of topological electronic materials. *arXiv preprint arXiv:1807.08756*
168. Vergniory M, Elcoro L, Felser C, Bernevig B, Wang Z. 2018. The (high quality) topological materials in the world. *arXiv preprint arXiv:1807.10271*
169. Tang F, Po HC, Vishwanath A, Wan X. 2018. Towards ideal topological materials: Comprehensive database searches using symmetry indicators. *arXiv preprint arXiv:1807.09744*